Received: 7 June 2023 | Revised: 17 December 2023 | Accepted: 29 February 2024

DOI: 10.1002/zamm.202300442

ZAMM

ORIGINAL PAPER

Electroosmotic microchannel flow of blood conveying copper and cupric nanoparticles: Ciliary motion experiencing entropy generation using backpropagated networks

Parikshit Sharma[1] | **Bhupendra K. Sharma**[1] | **Nidhish K. Mishra**[2] | **Bandar Almohsen**[3] | **Muhammad M. Bhatti**[4,5]

[1]Department of Mathematics, Birla Institute of Technology and Science, Pilani, Pilani, Rajasthan, India

[2]Department of Basic Science, College of Science and Theoretical Studies, Saudi Electronic University, Riyadh, Saudi Arabia

[3]Department of Mathematics, College of Science, King Saud University, Riyadh, Saudi Arabia

[4]College of Mathematics and Systems Science, Shandong University of Science and Technology, Qingdao, China

[5]Material Science, Innovation and Modelling (MaSIM) Research Focus Area, North-West University, Mafikeng Campus, Mmabatho, South Africa

Correspondence
Muhammad M. Bhatti, College of Mathematics and Systems Science, Shandong University of Science and Technology, Qingdao 266590, China.
Email: mmbhatti@sdust.edu.cn

Funding information
King Saud University

A novel mathematical model for a hybrid (Cu–CuO/blood) Jeffrey nanofluid passing a vertical symmetric microchannel along with an electroosmosis pump is presented. The focuses on the advancement of mathematical modeling techniques, its comprehensive analysis of microfluidic system dynamics, and its potential to inform the optimal design of devices using nanofluids with broad applications in various fields. Arrhenius's law is used to analyze endothermic–exothermic reactions and activation energy. The governing partial differential equations of the fixed frame are transformed into ordinary differential equations of the wave frame using self-similarity transformations. Low Reynolds number and long-wavelength approximations helped to find solutions of the equations by applying a suitable BVP solver in MATLAB. The fluid's velocity, temperature, concentration, and electroosmosis properties are studied graphically. Two-dimensional contour plots of fluid velocity and three-dimensional surface plots of fluid properties are discussed. Physically significant quantities of mass transfer rate, skin friction coefficient, entropy generation, and heat transfer rate are studied using contour plots. Artificial neural network simulation using Bayesian regularization backpropagation algorithms is analyzed for training state, error histogram, fit, performance, and regression plots. Conclusively, the comprehensive analysis of the fluid dynamics, entropy generation, mass and heat transfer, and in the microchannel, coupled with the successful implementation of artificial neural network simulation, contributes to an improved understanding of the system's behavior. Entropy generation was raised for enhanced Brownian motion number and reduced values of thermophoresis, activation energy, and endothermic–exothermic reaction parameters. This study's results can be used to improve the efficiency and effectiveness of microfluidic devices used in fields as diverse as electrical cooling and medicine delivery.

1 | INTRODUCTION

Nanofluids are liquids where the nanoscale particles are hanging in a base liquid. In a paper they published in 1995, Choi and Eastman [1] first described nanofluids. They found that nanoparticle suspension in the base liquid increased the temperature of the mixture, leading to the idea of using nanofluids as heat transfer fluids. Aytaç et al. [2] explored the usage of a water gatherer with a $MgO–CuO/H_2O$ hybrid nanoliquid, analyzing its impacts on heat transfer efficiency. Farooq et al. [3] created a computational framework to simulate a radiative hybrid nanofluid on a shrinking or stretching surface with entropy production. The influence of hybrid nanofluid pull–push on heat transfer and fluid flow over parallel surfaces was studied numerically and analytically by Abdollahi et al. [4]. The transformation of mechanical to internal heat energy resulting from frictional force experienced by a fluid as it moves through a channel or over a surface is called viscous dissipation. Using heat radiation and viscous dissipation, Kho et al. [5] investigated magnetohydrodynamic behavior of an $Ag–TiO_2$ hybrid nano liquid via a porous wedge. Using an optimization technique, Manzoor et al. [6] investigated the entropy optimization of the Marangoni flow of a hybrid nanofluid under the influence of viscous dissipation and activation energy, with melting phenomena. Joule heating is the heat generated when an electric current travels through a nanofluid due to the fluid's resistance. Raju [7] investigates micropolar and hybrid nanofluids' dynamical dissipative and radiative flow of nanofluids with relative irreversibility along a Joule-heating inclined channel. Ramesh et al. [8] offer ANN models of hybrid nanofluids alongside Ohic heating and magnetorheological radiation effects.

An inclined magnetic field can provide a Lorentz force, improving nanofluids' fluid flow. The magnetic field interacts with the charged particles in the fluid, producing propelling force in a specific direction. Selimefendigil and Öztop [9] looked into the behavior of several porous cylinders and an angled unfirm magnetic strength on forced convection of a hybrid nano liquid and discovered that these characteristics improve heat transfer performance. Vijayalakshmi and Sivaraj [10] investigated the effects of an inclinational magnetic field and radiation on the heat transport characteristics of a micropolar alumina–silica–water nanofluid in a square cavity. Gravitational acceleration can greatly impact the flow of nanofluids, especially in natural convection. When a nanofluid is heated, it loses density and rises due to gravity's buoyant force. Surendar and Muthtamilselvan [11] offered a gravitational quasiperiodic sinusoidal modulation approach for reducing chaos in an Ag–MgO/H2O hybrid nanofluid actuator and sensor array system. Rana et al. [12] looked at the thermal instability of a magneto-hybrid nanofluid layer sandwiched between rough surfaces with varying gravity and a space-dependent heat source. By boosting the heat transfer rate and decreasing the pressure drop, highly porous media can improve the performance of nanofluid flow. It increases the heat transfer surface area and is a filter to catch nanoparticles. Khosravi et al. [13] used a hybrid nanofluid to estimate entropy generation in a combined high-concentration solar panel with a microchannel heat sink with porous fins. Rashad et al. [14] investigated the effects of the flow of a magnetic Eyring–Powell hybrid nanofluid in a porous media that generates thermal radiation and heat production. By producing an electric field that causes the charged nanoparticles to move and increase their dispersion within the fluid, electroosmosis can be utilized to improve heat transfer performance and flow stability in nanofluid flow. Sridhar et al. [15] used entropy analysis to investigate the blood–copper/platinum nanofluid thermal and electroosmotic transfer in a microfluidic device. Blood flow changes due to electroosmotic forces of fractional ternary nanofluid during slip circumstances were investigated by Shahzadi et al. [16].

Heat transfer enhancement can be examined using a nanofluid flow heat source. The heat transfer rate could be improved and made more efficient by including a heat source in the nanofluid flow. Sajid et al. [17] used a unique tetra hybrid Tiwari and Das nanofluid model to investigate the flow of magnetized cross-tetra hybrid nanofluid via a stenosed artery with a nonuniform heat source (sink) and thermal radiation. Mahmood and Khan [18] studied the turbulent flow of a polymer-based ternary-hybrid nanofluid past a stretching surface equipped with suction and a heat source. Thermophoresis is the movement of particles in a fluid caused by a temperature gradient. Thermophoresis can be used to control the motion and deposition of nanoparticles in nanofluid flow. Abbas et al. [19] performed a computational analysis of the Marangoni convective flow of a hybrid nanofluid across an infinite disc with particle deposition by thermophoresis. Researchers Madhukesh et al. [20] studied the thermophoretic action and the impacts of convective heat on a hybrid nanofluid as it moved across a tiny needle. Brownian motion is significant in nanofluid flow because it affects particle distribution and transport parameters. Because of the small size of the nanoparticles, Brownian motion is the major mechanism of particle dispersion in nanofluids. Rashid et al. [21] demonstrated a homotopic solution to a hybrid nanofluid's chemically reactive magnetohydrodynamic flow across a rotating disc with Brownian motion and thermophoresis effects. Kalpana et al. [22] used a computer method to study the magnetohydrodynamic boundary layer flow of a hybrid nanofluid exhibiting thermophoresis and Brownian motion in a nonuniform channel.

Chemical reactions can influence nanofluid flow by changing fluid characteristics and the heat transfer mechanism. This can substantially impact the system's convective heat transfer coefficient and thermal performance. Ramzan et al.

[23] modeled the Cattaneo–Christov heat flux and Hall current in an engine oil engineering cross-hybrid nanofluid with an autocatalytic chemical reaction. Using a stretching sheet, a chemical reaction, and mobile microorganisms, Shah et al. [24] study the bio-convection effects of Prandtl hybrid nanofluid flow. Endothermic reactions take heat from their surroundings, resulting in a drop in temperature. Exothermic processes, on the other hand, release heat into the surrounding environment, increasing its temperature. Ullah et al. [25] investigated entropy creation in an endothermic/exothermic chemical reaction and magnetic nanofluid flow across a curved region with porous medium and variable permeability. To reduce the entropy produced by higher-order endothermic/exothermic chemical reactions requiring activation energy, Sharma et al. [26] employed MHD mixed convective flow across a stretching surface. The activation energy determines how quickly chemical reactions can take place in a moving nanofluid. The activation energy is the lowest possible activation energy for a chemical process. The activation energy of Arrhenius and the efficiency of convective heat transfer in radiative hybrid nanofluid flow are investigated by Jayaprakash et al. [27]. Raza et al. [28] investigated the dynamic behavior of mono- and hybrid nanofluids passing through porous surfaces while subjected to a binary chemical reaction, uniform magnetic strength, and activation energy. Haq et al. [29] performed a computational investigation of MHD Darcy–Forchheimer hybrid nanofluid flow across a stretching surface under the impact of the chemical reaction and activation energy.

Nonmagnetic particles, such as microspheres or nanoparticles, can be employed in blood flow studies as tracers or imaging agents. These particles do not respond to magnetic fields, allowing for their controlled introduction into the bloodstream to visualize and analyze flow patterns, study vascular dynamics, or track drug delivery within the circulatory system. Their inert nature ensures minimal interference with the physiological properties of blood while providing valuable insights for medical and research purposes. Rani et al. [30] introduce a reversible polypropylene waste-based sensor for detecting copper ions in blood and water, presenting an environmentally friendly approach with potential applications in environmental monitoring and healthcare. JP et al. [31] propose a zirconium copper oxide micro flowers-based nonenzymatic electrochemical sensor for glucose detection in saliva, urine, and blood serum, showcasing a versatile diagnostic tool with potential applications in point-of-care testing and continuous glucose monitoring. Khan et al. [32] provide knowledge of the dynamics of transient blood-carrying gold nanoparticles, considering significant factors such as entropy generation and Lorentz force. This study contributes to the understanding of the complex interactions between nanoparticles and blood components, with potential implications for biomedical applications. Rana et al. [33] investigate the energy system dynamics of a conductive solid body with bottom circular heaters, Ag–MgO (50:50)/water hybrid nanofluid, finite element, and neural computations for a comprehensive analysis. Rana et al. [34] explore the impact of different configurations involving heated elliptical bodies, fins, and a differential heater on magnetohydrodynamic convective transport within an inclined cavity, employing a hybrid nano liquid, with artificial neural network predictions aiding in the understanding of the phenomena.

A feedforward neural network is an artificial neural network in which information goes only one way, from the input layer to the output layer. It comprises three layers: an input layer, one or more hidden layers, and an output layer. Each layer comprises numerous neurons that receive input from the previous layer and produce output that is passed on to the following layer. The weights associated with the connections between neurons are modified during training to optimize the network's performance. When it comes to using neural networks, backpropagation is the supervised learning method of choice. To update the network's weights, the technique computes the gradient of the loss function with respect to the weights. First, the network is run forward with the input data to generate an output, and then, in a second pass, the network is run backwards with the difference between the generated output and the desired output to adjust the weights. Figure 1 depicts the study's simple feedforward network architecture with a backpropagation solver.

The Bayesian Regularization Backpropagation (BRBP) algorithm is a neural network training method that adjusts the regularization parameter during training using Bayesian inference. This enables the algorithm to change the network's complexity automatically and minimize overfitting. The BRBP algorithm changes the weights based on the gradient of the error function and the weights' estimated posterior probability, which is derived using a prior distribution and the data likelihood. The study employed MATLAB as the software for analysis, leveraging the BRBP algorithm for neural network simulation. The comprehensive list of weights and biases in this algorithm constitutes a set of optimized parameters crucial for accurate predictions, illustrating the intricate adjustments made during the training process to enhance the model's performance and predictive capabilities. The BRBP algorithm finds the training weight values experientially during the model training.

To predict data, the Bayesian regularization approach is used in conjunction with the binary sigmoid (logsig) activation function and the linear (purelin) function used in this study. The choice of activation functions in this study, specifically the binary sigmoid (logsig) and linear (purelin) functions, is underpinned by a strategic rationale. The binary sigmoid function, characterized by its sigmoidal shape, is well-suited for binary classification tasks, offering a smooth transition

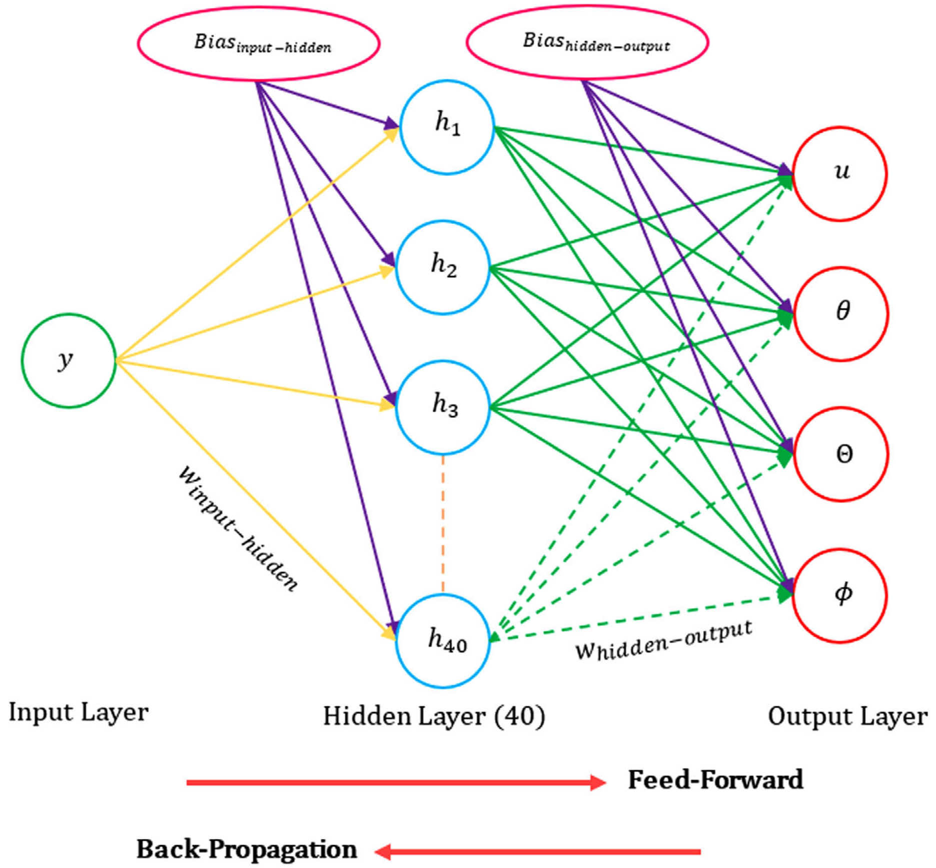

FIGURE 1 Feed-forward network architecture with a backpropagation solver.

between 0 and 1. Its nonlinearity facilitates the neural network's ability to capture complex relationships within the data. Complementing this, the linear function, purelin, is employed to ensure a straightforward linear combination of inputs, allowing the model to capture linear patterns effectively. The combination of these activation functions, when integrated with the Bayesian regularization method, aims to strike a balance between nonlinearity and linear adaptability, optimizing the neural network's predictive capacity across diverse data patterns and structures. The selection of these architectural parameters involves a delicate balance; too few neurons or layers may result in inadequate model complexity to capture intricate patterns, while an excessive number could lead to overfitting. The number of neurons and layers is experimentally selected here. Here, it is 40 in number, which is experimentally selected by the authors based on the literature review and hit-and-try method in MATLAB.

A study by Kanti et al. [35] showed that a Bayesian-optimized neural network with K-cross-fold validation can be used to predict the thermophysical properties of graphene oxide and MXene hybrid nanofluids for use in renewable energy applications. An artificial neural network trained with Bayesian regularization is used by Çolak [36] to predict the effects of viscous dissipation on the magnetohydrodynamic heat transfer flow of a copper-polyvinyl alcohol Jeffrey nanofluid across a stretchy surface. For the thermo-physical investigation of 3D MHD nanofluidic flow over an exponentially stretched surface, Awan et al. [37] provided a Bayesian regularization knack-based intelligent network. To represent the peristaltic motion of a third-grade fluid in a planar channel, Mahmood et al. [38] created adaptive Bayesian regularization networks. Shoaib et al. [39] provided a BRBP approach based on an intelligent computer system to investigate the viscous dissipative transport of a ferrofluid (Fe_3O_4) model. Artificial neural networks have been used in a variety of applications related to nanofluids, including the prediction of entropy generation [40], heat transfer performance [41], optimization of nanofluid properties [42], prediction of viscosity [43], cooling towers [44], and engines [45].

Considering the preceding insightful literature review, the authors believe that there is no published research work on cilia-regulated hybrid nanofluid (Cu–CuO/blood) with the effects of electroosmotic MHD, Joule heating, viscous dissipation, thermophoresis, Brownian motion, activation energy, and endothermic-exothermic chemical reactions in a vertical channel. The novelty of the present study is as follows:

- Entropy generation analysis for cilia-regulated hybrid nanofluid (Cu–CuO/blood) flow through a highly porous microchannel
- Investigated activation energy, an inclined external magnetic field, Brownian motion, endothermic-exothermic reactions, gravity, heat source or sink, highly porous medium, thermophoresis, and viscous dissipation effects.
- Scrutinization of the physical significance quantities of mass transfer rate, heat transfer rate, skin friction coefficient, entropy generation, and Bejan number.
- The BRBP algorithm is used to predict the velocity, temperature, concentration, and electroosmosis properties of the fluid.

2 | PROBLEM FORMULATION

Contemplate a hybrid nanofluid composed of Cu–CuO–blood, exhibiting symmetry, incompressibility, laminar flow, steadiness, pseudoplasticity, and thermal and electrical conductivity, according to the Jeffrey model. Cartesian coordinates are considered in the mathematical formulation of the model. The vertical direction is represented by the X^*-axis, while the horizontal direction is represented by the Y^* axis. The fluid is flowing in the positive X^*-axis direction. The space within the cilia walls is permeable, characterized by the permeability constant k_1. An external uniform magnetic field is applied to the flow. The magnetic field possesses a magnitude represented by B_0 and acts at an inclination of ω to the flow direction. Gravitational acceleration acts on the flow. The flow is considered under viscous dissipation when the fluid propagates. A heat source is present with the q_0 denoting the heat source or heat sink that is, $q_0 < 0$ represents heat sink and $q_0 > 0$ represents the heat source. The Arrhenius law incorporates endothermic and exothermic chemical reactions with activation energy into equations involving heat energy and concentration. The walls of cilia contain negative charges are located on the inner side, while positive charges are situated on the outer side. The channel is formed through the application of an axial electric field E_x. According to Sleigh's experimental research [46], the cilia are thought to follow elliptical motion pathways, hence the horizontal positions are mathematically expressed as

$$X^* = g\left(X^*, X_0^*, t^*\right) = X_0 + dl\alpha \sin\left[\frac{2\pi}{\lambda}\left(X^* - ct^*\right)\right] \tag{1}$$

The mathematical representation of the symmetrical metachronal undulating walls of a microchannel is articulated through their geometry:

$$H^* = f\left(X^*, t^*\right) = d + dl\cos\left[\frac{2\pi}{\lambda}\left(X^* - ct^*\right)\right] \tag{2}$$

The components in both the horizontal and vertical directions of the flow velocity at the electroosmotic pump microchannel walls can be calculated using the chain rule as follows:

$$W^* = \left(\frac{\partial X^*}{\partial t^*}\right)_{X_0} = \frac{\partial g}{\partial t^*} + \frac{\partial g}{\partial X^*}\frac{\partial X^*}{\partial t^*} = \frac{\partial g}{\partial t^*} + \frac{\partial g}{\partial X^*}W^*,\ U^* = \left(\frac{\partial H^*}{\partial t^*}\right)_{X_0} = \frac{\partial f}{\partial t^*} + \frac{\partial f}{\partial X^*}\frac{\partial X^*}{\partial t^*} = \frac{\partial f}{\partial t^*} + \frac{\partial f}{\partial X^*}W^* \tag{3}$$

Equation (3) can be further solved using Equations (1) and (2) and can be obtained in this form:

$$W^* = \frac{-\left(\frac{2\pi}{\lambda}\right)\left\{l\alpha dc\cos\left[\frac{2\pi}{\lambda}\left(X^* - ct^*\right)\right]\right\}}{1 - \left(\frac{2\pi}{\lambda}\right)\left\{l\alpha d\cos\left[\frac{2\pi}{\lambda}\left(X^* - ct^*\right)\right]\right\}},\ U^* = \frac{\left(\frac{2\pi}{\lambda}\right)\left\{ldc\sin\left[\frac{2\pi}{\lambda}\left(X^* - ct^*\right)\right]\right\}}{1 - \left(\frac{2\pi}{\lambda}\right)\left\{l\alpha d\cos\left[\frac{2\pi}{\lambda}\left(X^* - ct^*\right)\right]\right\}} \tag{4}$$

The Cauchy stress tensor T and additional stress tensor S, in the context of an incompressible Jeffrey fluid, are articulated as per [47].

$$T = -PI + S,\ S = \frac{\mu_{hnf}}{1+\lambda_1}\left(\dot{\gamma} + \lambda_2^*\frac{d\dot{\gamma}}{dt^*}\right) \tag{5}$$

where P is the pressure, and I is the identity tensor. The hybrid nanofluid flow problem to be investigated in this study is illustrated in Figure 2. Building upon the work of Ying-Qing et al. [48] and Cao et al. [49], we incorporated modifications to

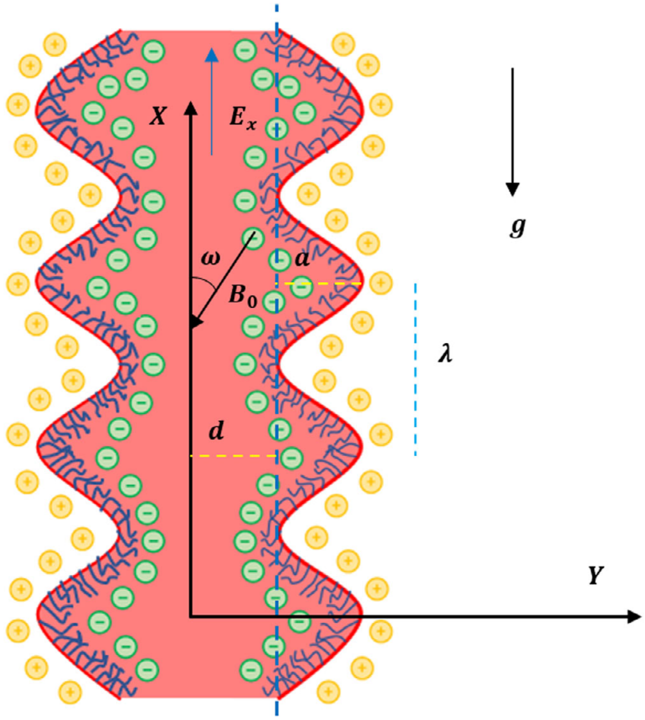

FIGURE 2 Geometrical description of the cilia problem.

Buongiorno's Nanofluid Model in both the energy and concentration equations. This adjustment accounts for the effects of thermo-migration and the random motion of nanoparticles, which arise from changes in concentration. The governing equations of this fluid with the environment mentioned above are written in the following fashion [42, 43]:

Continuity equation:

$$\frac{\partial U^*}{\partial X^*} + \frac{\partial W^*}{\partial Y^*} = 0 \tag{6}$$

Momentum equations:

$$\rho_{hnf}\left[\frac{\partial U^*}{\partial t^*} + U^*\frac{\partial U^*}{\partial X^*} + W^*\frac{\partial U^*}{\partial Y^*}\right] = -\frac{\partial P^*}{\partial X^*} + \frac{\partial S^*_{X^*X^*}}{\partial X^*} + \frac{\partial S^*_{X^*Y^*}}{\partial Y^*} + \rho_{hnf} g\beta_t (1-C_0)(T^*-T_0)$$
$$-\left(\rho_p-\rho_f\right) g\beta_c (C^*-C_0) - \sigma_{hnf} B_0^2 U^* \sin^2\omega - \frac{\mu_{hnf}}{k_1}U^* - F_0 U^{*2} + \rho_e E_x \tag{7}$$

$$\rho_{hnf}\left[\frac{\partial W^*}{\partial t^*} + U^*\frac{\partial W^*}{\partial X^*} + W^*\frac{\partial W^*}{\partial Y^*}\right] = -\frac{\partial P^*}{\partial Y^*} + \frac{\partial S^*_{X^*Y^*}}{\partial X^*} + \frac{\partial S^*_{Y^*Y^*}}{\partial Y^*} - \frac{\mu_{hnf}}{k_1}W^* - F_0 W^{*2} \tag{8}$$

Energy equation:

$$\left(\rho c_p\right)_{hnf}\left[\frac{\partial T^*}{\partial t^*} + U^*\frac{\partial T^*}{\partial X^*} + W^*\frac{\partial T^*}{\partial Y^*}\right] = k_{hnf}\left(\frac{\partial^2 T^*}{\partial X^{*2}} + \frac{\partial^2 T^*}{\partial Y^{*2}}\right) + \left[S^*_{X^*X^*}\frac{\partial U^*}{\partial X^*} + S^*_{X^*Y^*}\left(\frac{\partial U^*}{\partial Y^*} + \frac{\partial W^*}{\partial X^*}\right) + S^*_{Y^*Y^*}\frac{\partial W^*}{\partial X^*}\right]$$
$$+\tau\left(\rho c_p\right)_{hnf}\left[D_B\left(\frac{\partial T^*}{\partial X^*}\frac{\partial C^*}{\partial X^*} + \frac{\partial T^*}{\partial Y^*}\frac{\partial C^*}{\partial Y^*}\right) + \frac{D_T}{T_0}\left\{\left(\frac{\partial T^*}{\partial X^*}\right)^2 + \left(\frac{\partial T^*}{\partial Y^*}\right)^2\right\}\right]$$
$$+\sigma_{hnf} B_0^2 \sin^2\omega U^{*2} + q_o (T^*-T_0) + k_r^2 \varsigma (C^*-C_0) R_c \tag{9}$$

TABLE 1 Presents the thermophysical characteristics of Cu–CuO/blood.

Properties	Notation	Nanoparticle Cu	Nanoparticle CuO	Base fluid Blood
Specific heat (J/Kg K)	C_p	385	540	3617
Density (Kg/m^3)	ρ	8933	6510	1150
Thermal conductivity (W/m K)	k	400	18	0.53

Concentration equation:

$$\frac{\partial C^*}{\partial t^*} + U^* \frac{\partial C^*}{\partial X^*} + W^* \frac{\partial C^*}{\partial Y^*} = D_B \left(\frac{\partial^2 C^*}{\partial X^{*2}} + \frac{\partial^2 C^*}{\partial Y^{*2}} \right) + \frac{D_T}{T_0} \left(\frac{\partial^2 T^*}{\partial X^{*2}} + \frac{\partial^2 T^*}{\partial Y^{*2}} \right) - k_r^2 \left(C^* - C_0 \right) R_c \tag{10}$$

Poisson–Boltzmann equation:

$$\frac{\partial^2 \phi^*}{\partial X^{*2}} + \frac{\partial^2 \phi^*}{\partial Y^{*2}} = -\frac{\rho_e}{\varepsilon \varepsilon_0} \tag{11}$$

With the following boundary conditions:

$$\left. \begin{array}{l} U^* = -\dfrac{\left(\frac{2\pi}{\lambda}\right)\left\{ldcsin\left[\frac{2\pi}{\lambda}(X^*-ct^*)\right]\right\}}{1-\left(\frac{2\pi}{\lambda}\right)\left\{l\alpha dcos\left[\frac{2\pi}{\lambda}(X^*-ct^*)\right]\right\}},\ T^* = T_0\ ,\ C^* = C_0\ \ at\ \ Y^* = -H^* \\ \\ U^* = \dfrac{\left(\frac{2\pi}{\lambda}\right)\left\{ldc\sin\left[\frac{2\pi}{\lambda}(X^*-ct^*)\right]\right\}}{1-\left(\frac{2\pi}{\lambda}\right)\left\{l\alpha d\cos\left[\frac{2\pi}{\lambda}(X^*-ct^*)\right]\right\}}\ ,\ T^* = T_1\ ,\ C^* = C_1\ \ at\ \ Y^* = +H^* \end{array} \right\} \tag{12}$$

where g denotes the strength of gravitational acceleration, ρ_{hnf}, σ_{hnf}, μ_{hnf}, k_{hnf}, and $(C_p)_{hnf}$ are density, electrical conductivity, dynamic viscosity, thermal conductivity, and specific heat of the hybrid nanofluid, respectively. The thermophysical properties of the current hybrid nanofluid, along with their corresponding values, are detailed in Table 1 and are mathematically represented as per [50]:

$$\begin{gathered} \frac{\mu_{hnf}}{\mu_f} = \left[(1-\phi_{Cu})(1-\phi_{CuO})\right]^{-2.5}, \\ \frac{\rho_{hnf}}{\rho_f} = (1-\phi_{Cu}) \left[(1-\phi_{CuO}) + \phi_{CuO}\frac{\rho_{CuO}}{\rho_f}\right] + \phi_{Cu}\frac{\rho_{Cu}}{\rho_f}, \\ \frac{(\rho C_p)_{hnf}}{(\rho C_p)_f} = (1-\phi_{Cu}) \left[(1-\phi_{CuO}) + \phi_{CuO}\frac{(\rho C_p)_{CuO}}{(\rho C_p)_f}\right] + \phi_{Cu}\frac{(\rho C_p)_{Cu}}{(\rho C_p)_f} \\ \frac{\sigma_{hnf}}{\sigma_{nf}} = \left[\frac{\sigma_{CuO} + 2\sigma_{nf} - 2\phi_{CuO}\left(\sigma_{nf} - \sigma_{CuO}\right)}{\sigma_{CuO} + 2\sigma_{nf} + \phi_{CuO}\left(\sigma_{nf} - \sigma_{CuO}\right)}\right], \\ \frac{\sigma_{nf}}{\sigma_f} = \left[\frac{\sigma_{Cu} + 2\sigma_f - 2\phi_{Cu}\left(\sigma_f - \sigma_{Cu}\right)}{\sigma_{Cu} + 2\sigma_f + \phi_{Cu}\left(\sigma_f - \sigma_{Cu}\right)}\right], \\ \frac{k_{hnf}}{k_{nf}} = \left[\frac{k_{CuO} + 2k_{nf} - 2\phi_{CuO}\left(k_{nf} - k_{CuO}\right)}{k_{CuO} + 2k_{nf} + \phi_{CuO}\left(k_{nf} - k_{CuO}\right)}\right], \\ \frac{k_{nf}}{k_f} = \left[\frac{k_{Cu} + 2k_f - 2\phi_{Cu}\left(k_f - k_{Cu}\right)}{k_{Cu} + 2k_f + \phi_{Cu}\left(k_f - k_{Cu}\right)}\right], \\ \phi = \phi_{Cu} + \phi_{CuO} \end{gathered} \tag{13}$$

The fluid flow problem is converted from a fixed frame to a wave frame using the following transformations:

$$X^* = x^* + ct^*,\ \ Y^* = y^*,\ \ U^* = u^* + c,\ W^* = w^*,\ P^*\left(X^*, Y^*, t^*\right) = p\left(x^*, y^*\right),\ T^* = T,\ C^* = C \tag{14}$$

Now, to convert the dimensional PDEs into dimensionless PDEs, the following transformations are used:

$$x = \frac{x^*}{\lambda},\quad y = \frac{y^*}{d},\quad u = \frac{u^*}{c},\quad w = \frac{w^*}{c},\quad t = \frac{ct^*}{\lambda},\quad h = \frac{H}{d},\quad \delta = \frac{d}{\lambda},\quad p = \frac{d^2 p^*}{c\lambda\mu_f},\quad \lambda_2^* = \frac{c\lambda_2}{d},\quad S = \frac{S^* d}{c\mu_f},$$
$$\psi = \frac{\psi^*}{cd},\quad \phi = \frac{\phi *}{\zeta},\quad \theta = \frac{T^* - T_0}{T_1 - T_0},\quad \Theta = \frac{C^* - C_0}{C_1 - C_0},\quad \Omega = \frac{T_1 - T_0}{T_0},\quad ,\quad \Pi = \frac{\mathrm{C}_1 - \mathrm{C}_0}{\mathrm{C}_0} \tag{15}$$

In the context where dimensionless pressure is denoted by p, dimensionless temperature by θ, dimensionless concentration by Θ, electro-osmotic potential by ϕ, temperature ratio by Ω, and concentration ratio by Π, the rate constant for both endothermic and exothermic chemical reactions, characterized by activation energy R_c, is assumed to rely on the absolute temperature T^*. This relationship is expressed mathematically through the modified Arrhenius law [51]:

$$R_c = \left(\frac{T^*}{T_0}\right)^n e^{-\left(\frac{E_a}{k_b T^*}\right)}$$

After solving the Nernst–Planck equation and considering the effects of long wavelength, low Reynolds number, and low zeta potential, the electric charge density is determined according to the methodology outlined in Ref. [52]:

$$\rho_e = -\frac{2m_0 (ez)^2 \phi^*}{k_b T_{ave}}$$

After using the above-mentioned transformations (14–15) and substitutions, Equations (7)–(11) can be converted from dimensional PDEs to dimensionless ODEs as described below:

$$A_1 Re\delta\left[(1+u)\frac{\partial u}{\partial x} + \frac{w}{\delta}\frac{\partial u}{\partial y}\right] = -\frac{\partial p}{\partial x} + A_2\left(\delta\frac{\partial S_{xx}}{\partial x} + \frac{\partial S_{xy}}{\partial y}\right) + A_1 Gr\theta - Gc\Theta$$
$$- \left[A_3 M^2 \sin^2\omega + \frac{A_2}{Da} + ReFr\,(1+u)\right](1+u) + U_{HS}K^2\phi, \tag{16}$$

$$A_1 Re\delta^2\left[(1+u)\frac{\partial w}{\partial x} + \frac{w}{\delta}\frac{\partial w}{\partial y}\right] = -\frac{\partial p}{\partial y} + A_2\left(\delta^2\frac{\partial S_{xy}}{\partial x} + \delta\frac{\partial S_{yy}}{\partial y}\right) - A_2\delta\frac{w}{Da} - \delta ReFrw^2, \tag{17}$$

$$A_4 Re\delta\left[(1+u)\frac{\partial\theta}{\partial x} + \frac{w}{\delta}\frac{\partial\theta}{\partial y}\right]$$
$$= \frac{A_5}{Pr}\left(\delta^2\frac{\partial^2\theta}{\partial x^2} + \frac{\partial^2\theta}{\partial y^2}\right) + Ec\left[\left\{A_2\delta S_{xx}\frac{\partial u}{\partial x} + S_{xx}\left(\frac{\partial u}{\partial y} + \delta\frac{\partial w}{\partial x}\right) + \delta S_{yy}\frac{\partial w}{\partial y}\right\} + A_3 M^2 (1+u)^2 \sin^2\omega\right]$$
$$+Nb\left(\delta^2\frac{\partial\theta}{\partial x}\frac{\partial\Theta}{\partial x} + \frac{\partial\theta}{\partial y}\frac{\partial\Theta}{\partial y}\right) + Nt\left[\delta^2\left(\frac{\partial\theta}{\partial x}\right)^2 + \left(\frac{\partial\theta}{\partial y}\right)^2\right] + Q\theta + Kr_1 Kr_2\Theta(1+\Omega\theta)^n e^{-\left(\frac{E^*}{1+\Omega\theta}\right)}, \tag{18}$$

$$ScRe\delta\left[(1+u)\frac{\partial\Theta}{\partial x} + \frac{w}{\delta}\frac{\partial\Theta}{\partial y}\right] = \left(\delta^2\frac{\partial^2\Theta}{\partial x^2} + \frac{\partial^2\Theta}{\partial y^2}\right) + \frac{Nt}{Nb}\left(\delta^2\frac{\partial^2\theta}{\partial x^2} + \frac{\partial^2\theta}{\partial y^2}\right) - Kr_1 Sc\Theta(1+\Omega\theta)^n e^{-\left(\frac{E^*}{1+\Omega\theta}\right)}, \tag{19}$$

$$\delta^2\frac{\partial^2\phi}{\partial x^2} + \frac{\partial^2\phi}{\partial y^2} = K^2\,\phi \tag{20}$$

A_{1-4} denote the ratios of thermophysical properties in hybrid nanofluid to those in the base fluid. They are specified as

$$A_1 = \frac{\rho_{hnf}}{\rho_f},\ A_2 = \frac{\mu_{hnf}}{\mu_f},\ A_3 = \frac{\sigma_{hnf}}{\sigma_f},\ A_4 = \frac{(\rho c_p)_{hnf}}{(\rho c_p)_f},\ A_5 = \frac{k_{hnf}}{k_f}$$

where Gr (thermal Grashof number) $= \frac{\rho_f g \beta_t (1-C_0)(T-T_0)d^2}{\mu_f c}$, Gc (solutal Grashof number) $= \frac{(\rho_p-\rho_f) g\beta_c (C^*-C_0)d^2}{\mu_f c}$, Re (Reynolds number) $= \frac{cd}{\upsilon_f}$, M (magnetic number) $= \sqrt{\frac{\sigma_f}{\mu_f}} B_0 d$, Da (Darcy number) $= \frac{k_1}{d^2}$, Fr (Forchheimer number) $= \frac{F_0 d}{\rho_f}$, Ec (Eckert number) $= \frac{c^2}{(c_p)_f (T_1-T_0)}$, Pr (Prandtl number) $= \frac{\mu_f (c_p)_f}{k_f}$, Nb (Brownian motion parameter) $= \frac{\tau D_B (C_1-C_0)}{\upsilon_f \Delta C}$, Nt (thermophoresis parameter) $= \frac{\tau D_T (T_1-T_0)}{T_0 \upsilon_f}$, K (electroosmotic parameter) $= dze\sqrt{\frac{2m_0}{k_b T_{ave}\varepsilon\varepsilon_0}}$, U_{HS} (Helmholtz–Smoluchowski velocity) $= -\frac{E_x \varepsilon\varepsilon_0 \zeta}{\mu_f c}$, Kr_1 (chemical reaction parameter) $= \frac{k_r^2 d^2}{\upsilon_f}$, Kr_2 (endothermic–exothermic reaction parameter) $= \frac{\varsigma}{(\rho c_p)_f}\left(\frac{C_1-C_0}{T_1-T_0}\right)$, E^* (activation energy parameter) $= \frac{E_a}{K_b T_0}$, Br (Brinkman number) $= PrEc$, Sc (Schmidt number) $= \frac{\upsilon_f}{D_B}$, Q (heat generation parameter) $= \frac{q_o d^2}{(\rho c_p)_f \upsilon_f}$, Le (Lewis number) $= \frac{k_f}{D_B C_0}$.

Now, we would use the stream function ψ satisfying the continuity equation as

$$u = \frac{\partial \psi}{\partial y} \text{ and } w = -\delta \frac{\partial \psi}{\partial x}$$

Therefore, the stress components are represented by the following form:

$$S_{xx} = \frac{2\delta\mu_f}{1+\lambda_1}\left[1 + \frac{\lambda_2 c\delta}{d}\left(\frac{\partial\psi}{\partial y}\frac{\partial}{\partial x} - \frac{\partial\psi}{\partial x}\frac{\partial}{\partial y}\right)\right]\frac{\partial}{\partial y}\left(\frac{\partial\psi}{\partial x}\right),$$

$$S_{xy} = \frac{\mu_f}{1+\lambda_1}\left[1 + \frac{\lambda_2 c\delta}{d}\left(\frac{\partial\psi}{\partial y}\frac{\partial}{\partial x} - \frac{\partial\psi}{\partial x}\frac{\partial}{\partial y}\right)\right]\left(\frac{\partial^2\psi}{\partial y^2} - \delta\frac{\partial^2\psi}{\partial x^2}\right),$$

$$S_{yy} = \frac{2\delta\mu_f}{1+\lambda_1}\left[1 + \frac{\lambda_2 c\delta}{d}\left(\frac{\partial\psi}{\partial y}\frac{\partial}{\partial x} - \frac{\partial\psi}{\partial x}\frac{\partial}{\partial y}\right)\right]\frac{\partial}{\partial y}\left(\frac{\partial\psi}{\partial x}\right)$$

Applying the long wavelength ($\lambda \to \infty$, $\delta \to 0$) and low Reynolds number ($Re \to 0$) approximations to the stress components and dimensionless governing equations mentioned above, Equations (16)–(20) become

$$\frac{\partial p}{\partial x} = \frac{A_2}{1+\lambda_1}\frac{\partial^3\psi}{\partial y^3} + A_1 Gr\theta - Gc\Theta - \left[A_3 M^2 \sin^2\omega + \frac{A_2}{Da} + ReFr\left(1 + \frac{\partial\psi}{\partial y}\right)\right]\left(1 + \frac{\partial\psi}{\partial y}\right) + U_{HS} K^2 \phi, \tag{21}$$

$$\frac{\partial p}{\partial y} = 0, \tag{22}$$

$$A_5 \frac{\partial^2\theta}{\partial y^2} + Br\left[\frac{A_2}{1+\lambda_1}\left(\frac{\partial^2\psi}{\partial y^2}\right)^2 + A_3 M^2 \left(1 + \frac{\partial\psi}{\partial y}\right)^2 \sin^2\omega\right]$$
$$+ PrNb\frac{\partial\theta}{\partial y}\frac{\partial\Theta}{\partial y} + PrNt\left(\frac{\partial\theta}{\partial y}\right)^2 + Q\theta + PrKr_1 Kr_2 \Theta (1+\Omega\theta)^n e^{-\left(\frac{E^*}{1+\Omega\theta}\right)} = 0, \tag{23}$$

$$\frac{\partial^2\Theta}{\partial y^2} + \frac{Nt}{Nb}\frac{\partial^2\theta}{\partial y^2} - Kr_1 Sc\Theta(1+\Omega\theta)^n e^{-\left(\frac{E^*}{1+\Omega\theta}\right)} = 0, \tag{24}$$

$$\frac{\partial^2\phi}{\partial y^2} = K^2\phi \tag{25}$$

Equation (22) is trivially satisfied. From Equation (21), the pressure gradient w.r.t x is eliminated via cross-difference, that is, by taking the first derivative w.r.t y on both sides. The final equation is obtained as follows:

$$A_2\frac{\partial^4\psi}{\partial y^4}-\left[A_3M^2\sin^2\omega+\frac{A_2}{Da}+2ReFr\left(1+\frac{\partial\psi}{\partial y}\right)\right]\frac{\partial^2\psi}{\partial y^2}+A_1Gr\frac{\partial\theta}{\partial y}-Gc\frac{\partial\Theta}{\partial y}+U_{HS}K^2\frac{\partial\phi}{\partial y}=0 \tag{26}$$

With the following boundary conditions:

$$\left.\begin{aligned}\psi&=+\tfrac{F}{2},\ \frac{\partial\psi}{\partial y}=-1-\frac{2\pi l\delta\sin(2\pi x)}{1-2\pi l\alpha\delta\cos(2\pi x)},\theta=0,\Theta=0,\phi=\zeta_1\,,at\ y=-h,\\ \psi&=-\tfrac{F}{2},\ \frac{\partial\psi}{\partial y}=-1+\frac{2\pi l\delta\sin(2\pi x)}{1-2\pi l\alpha\delta\cos(2\pi x)},\theta=1,\Theta=1,\phi=\zeta_2\,,at\ y=+h\end{aligned}\right\} \tag{27}$$

Below, the relevant physical quantities are defined. This study investigates quantities such as heat transfer rate, mass transfer rate, and coefficients related to shear stress or drag force for the specified hybrid nanofluid. The mathematical expressions for the Nusselt number, skin friction coefficient, and Sherwood number are provided as follows [53]:

$$Nu=\frac{dq_w}{k_f\left(T_1-T_0\right)},\ \ C_f=\frac{\tau_u}{\rho_f c^2},\ Sh=\frac{dm_w}{\rho_f D_B\left(C_1-C_0\right)} \tag{28}$$

where, q_w is the heat flux, τ_u is the axial stress, and m_w is the mass flux. They are defined as

$$q_w=-k_{hnf}\left(\frac{\partial T^*}{\partial Y^*}\right)_{Y^*=0},\ \ \tau_u=\frac{\mu_{hnf}}{1+\lambda_1}\left(\frac{\partial U^*}{\partial Y^*}\right)_{Y^*=0},\ \ m_w=-\rho_f D_B\left(\frac{\partial C^*}{\partial Y^*}\right)_{Y^*=0} \tag{29}$$

Equation (29) is used to convert Equation (28) into their nondimensional form as

$$Nu=-A_5\theta'(0),\ C_fRe=A_2\frac{1}{1+\lambda_1}u'(0),\ Sh=-\Theta'(0) \tag{30}$$

Next, an analysis of entropy generation will be conducted for the previously mentioned hybrid nanofluid. It is assumed that the primary contributors to entropy in the channel are the effects of mass transfer, viscous dissipation, Joule heating, friction, and heat transfer. In accordance with the second law of thermodynamics, the expression for entropy in the wave frame is as follows [54]:

$$\begin{aligned}S_{gen}=&\frac{k_{thnf}}{T_0^2}\left(\nabla T^*\right)^2+\frac{\mu_{thnf}}{T_0}\left(\frac{\partial^2\psi^*}{\partial y^{*2}}\right)^2+\frac{\mu_{thnf}}{T_0}\left(\frac{1}{1+\lambda_1}\right)\left(\frac{\partial^2\psi^*}{\partial y^{*2}}\right)^2\\&+\frac{\sigma_{thnf}B_0^2\sin^2\omega}{T_0}\left(c+\frac{\partial\psi^*}{\partial y^*}\right)^2+\frac{D_B}{C_0}\left(\nabla C^*\right)^2+\frac{D_B}{T_0}\left(\nabla T^*\nabla C^*\right)\end{aligned} \tag{31}$$

By substituting Equations (14) and (15) into Equation (31), we obtain the characteristic entropy, lubrication approximations, and the expression for the total entropy generation number as follows:

$$N_G=\underbrace{A_5\left(\frac{\partial\theta}{\partial y}\right)^2}_{N_T}+\underbrace{\frac{Br}{\Omega}\left(\frac{\partial^2\psi}{\partial y^2}\right)^2}_{N_V}+\underbrace{A_2\frac{Br}{\Omega}\left(\frac{1}{1+\lambda_1}\right)\left(\frac{\partial^2\psi}{\partial y^2}\right)^2}_{N_F}+\underbrace{A_3\frac{BrM^2\sin^2\omega}{\Omega}\left(1+\frac{\partial\psi}{\partial y}\right)^2}_{N_J}+\underbrace{\left(\frac{\Pi}{\Omega}\frac{\partial\Theta}{\partial y}\right)^2+\frac{\Pi}{\Omega Le}\left(\frac{\partial\theta}{\partial y}\frac{\partial\Theta}{\partial y}\right)}_{N_M} \tag{32}$$

N_T represents thermal irreversibility, N_V stands for viscous irreversibility, N_F denotes fluid friction irreversibility, N_J corresponds to Joule heating irreversibility, and N_M signifies mass transfer irreversibility. The Bejan number, denoted as Be, is a ratio that quantifies the irreversibility caused by heat transfer in relation to the total irreversibility. Mathematically, it is defined as

$$Be = \frac{A_5\left(\frac{\partial\theta}{\partial y}\right)^2}{A_5\left(\frac{\partial\theta}{\partial y}\right)^2 + \frac{Br}{\Omega}\left(\frac{\partial^2\psi}{\partial y^2}\right)^2 + A_2\frac{Br}{\Omega}\left(\frac{1}{1+\lambda_1}\right)\left(\frac{\partial^2\psi}{\partial y^2}\right)^2 + A_3\frac{BrM^2\sin^2\omega}{\Omega}\left(1+\frac{\partial\psi}{\partial y}\right)^2 + \left(\frac{\Pi}{\Omega}\frac{\partial\Theta}{\partial y}\right)^2 + \frac{\Pi}{\Omega Le}\left(\frac{\partial\theta}{\partial y}\frac{\partial\Theta}{\partial y}\right)} \tag{33}$$

3 | NUMERICAL SOLUTION

A convenient BVP solver is used to tackle the generated ODEs (23–26) and boundary conditions (27). The following are some substitutes:

$$\begin{aligned} &Y_1 = \psi, \quad Y_2 = \frac{\partial\psi}{\partial y}, \quad Y_3 = \frac{\partial^2\psi}{\partial y^2}, \quad Y_4 = \frac{\partial^3\psi}{\partial y^3}, \quad Y_5 = \theta, \quad Y_6 = \frac{\partial\theta}{\partial y}, \\ &Y_7 = \Theta, \quad Y_8 = \frac{\partial\Theta}{\partial y}, \quad Y_9 = \phi, \quad Y_{10} = \frac{\partial\phi}{\partial y}, \quad Y_6' = \xi_1, \end{aligned} \tag{34}$$

As a consequence of these replacements, an initial value problem composed of nine first-order differential equations emerges:

$$\left.\begin{aligned} Y_1' &= Y_2\,, \\ Y_2' &= Y_3\,, \\ Y_3' &= Y_4\,, \\ Y_4' &= \frac{\left[A_3M^2\sin^2\omega + \frac{A_2}{Da} + 2ReFr(1+Y_2)\right]Y_3 - A_1GrY_6 + GcY_8 - U_{HS}K^2Y_9}{\left(A_2 + \frac{1}{1+\lambda_1}\right)}\,, \\ Y_5' &= Y_6\,, \\ Y_6' &= \frac{-Br\left[A_2(Y_3)^2 + A_3M^2(1+Y_2)^2\sin^2\omega\right] - PrNbY_6Y_8 - PrNt(Y_6)^2 - QY_5 - PrKr_1Kr_2Y_7(1+\Omega Y_5)^n e^{-\left(\frac{E^*}{1+\Omega Y_5}\right)}}{A_5}\,, \\ Y_7' &= Y_8\,, \\ Y_8' &= -\frac{Nt}{Nb}\xi_2 + Kr_1ScY_7(1+\Omega Y_5)^n e^{-\left(\frac{E^*}{1+\Omega Y_5}\right)}, \\ Y_9' &= Y_{10}\,, \\ Y_{10}' &= K^2\,Y_9 \end{aligned}\right\} \tag{35}$$

With the following boundary conditions,

$$\left.\begin{aligned} &Y_1\,(-h) = \frac{F}{2}\,, Y_2\,(-h) = -1, Y_5\,(-h) = 0, Y_7\,(-h) = 0, Y_9\,(-h) = \zeta_1\,, \\ &Y_1\,(+h) = -\frac{F}{2}, Y_2\,(+h) = -1, Y_5\,(+h) = 1, Y_7\,(+h) = 1, Y_9\,(+h) = \zeta_2 \end{aligned}\right\} \tag{36}$$

The MATLAB function BVP5C is used to produce numerical results for Equation (35) using the boundary conditions of Equation (36).

4 | RESULTS VALIDATION

Figures 3a and 3b depict a comparative representation of u and θ. The current model aligns with a previously published study by Alla et al. [42], as evidenced in Figure 3a displaying the curve for a set of dimensionless parameters and Figure 3b

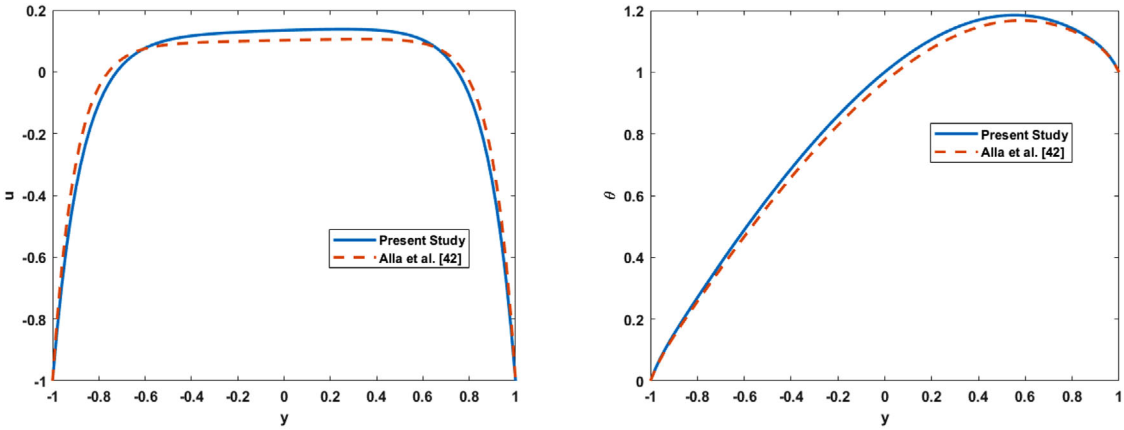

(a) *Comparative analysis of u* (b) *Comparative analysis of θ*

FIGURE 3 (a) Comparative analysis of $\boldsymbol{u}$. (b) Comparative analysis of θ.

illustrating the temperature curve. Both figures indicate the consistency between the present investigation and the earlier work. Subsequent sections delve into the specifics of this study, offering detailed insights. Various profiles, encompassing velocity, temperature, concentration, and induced magnetic field, are graphed for different combinations of dimensionless parameters. The ranges and references of nondimensional numbers obtained from the literature review conducted above are summarized in Table 2.

5 | RESULTS AND DISCUSSIONS

5.1 | Velocity profiles

Figure 4 illustrates the impact of magnetic field inclination, Reynolds number, copper concentration, and Helmholtz–Smoluchowski velocity parameters on the axial velocity. Figure 4a depicts the effect of magnetic field inclination on velocity. The magnetic field strength increases by enhancing the inclination angle, generating the Lorentz force. This Lorentz force provides more resistance to the nanoparticle's flow, decreasing the flow velocity. Figure 4b shows the impact of the Reynolds number on axial velocity. The figure shows that the velocity profiles go down by enhancing the Reynolds number. Physically, as the Reynolds number boosts up, the viscous force effect decreases, and the velocity profiles decrease for the flow. Figure 4c illustrates the effects of changes in copper concentration on the fluid's velocity. On increasing the copper concentration, the velocity decreases. This happens because, on increasing the copper nanoparticle amount in the fluid, the nanoparticles experience more resistance and the fluid experiences less velocity. Figure 4d represents the flow velocity change for Helmholtz–Smoluchowski velocity. This figure shows that by increasing the Helmholtz–Smoluchowski velocity, the velocity increases. Higher Helmholtz–Smoluchowski velocity strength reduces the viscoelastic effects and plays a crucial role in the acceleration of velocity values.

TABLE 2 References and ranges of flow parameters.

Parameter	Gr	Gc	Re	M	Da	U_{HS}	Br	Q	F	ϕ	Fr
Range	[0–8]	[0–8]	[0–8]	[0–10]	[0–1]	[0–20]	[0–5]	[−10,10]	[0–1]	[0–1]	[0–20]
Default	0.5	0.5	0.5	2	0.03	0.5	0.5	0.5	0.05	0.1	0.5
Reference	[60]	[60]	[56]	[55–65]	[61]	[64]	[57]	[55]	[65]	[59]	[61–66]

Parameter	λ_1	n	K	Ω	Sc	Nb	Nt	Kr_1	Kr_2	E
Range	[0–5]	[0–1]	[0–20]	[0–1]	[0–10]	[0–5]	[0–5]	[0–15]	[−10,10]	[−10,10]
Default	1	1	2	1	0.3	0.5	0.5	0.5	0.5	1
Reference	[42]	[63]	[64]	[58]	[58]	[62]	[62]	[63]	[63]	[63]

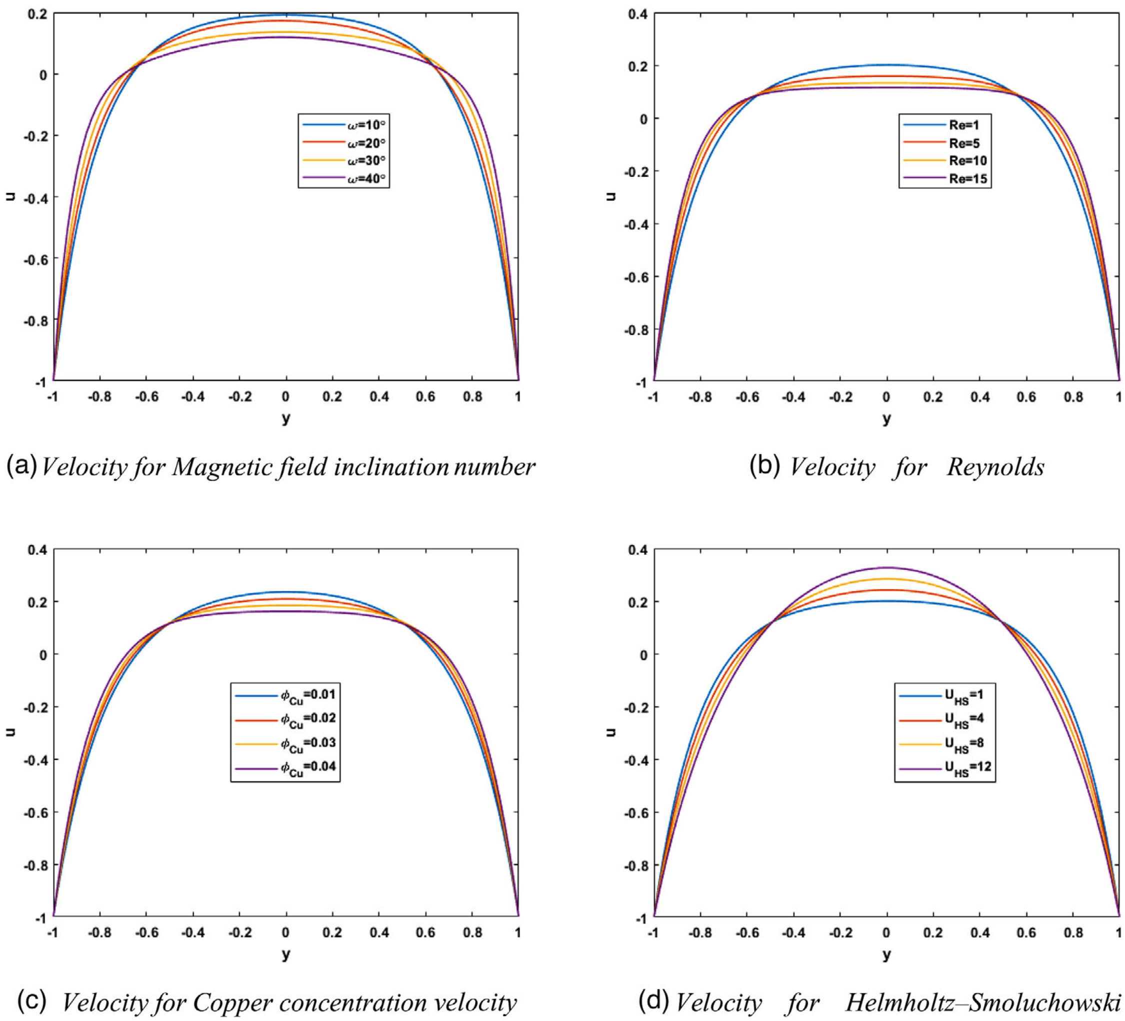

FIGURE 4 (a) Velocity for magnetic field inclination. (b) Velocity for Reynolds number. (c) Velocity for copper concentration. (d) Velocity for Helmholtz–Smoluchowski velocity.

5.2 | Temperature profiles

Figure 5 represents the impact of the Forchheimer number, temperature ratio, fitting constant, and activation energy parameter on the fluid's temperature profiles. Figure 5a shows the effect of the Forchheimer number on temperature. This shows that by increasing the Forchheimer number, the temperature of the fluid goes down. As the Forchheimer number increases, the porosity of the medium increases. Figure 5b depicts the effect of the temperature ratio parameter on the fluid temperature. On increasing the temperature ratio parameter, the temperature of the fluid increases. Figure 5c shows the effect of the fitting constant parameter on the temperature profiles. The temperature ratios increase and the fluid's temperature profiles increase with an increase in the fitting constant parameter. A temperature-fitting constant is used to adjust the viscosity and thermal conductivity of the nanofluid to account for these differences. Figure 5d represents the changes in activation energy parameters with temperature. The figure shows that the temperature profiles decrease with increasing activation energy. The activation energy is the lowest possible amount of energy required to initiate a chemical reaction. In other words, the energy barrier must be overcome to transform reactants into products.

5.3 | Concentration profiles

Figure 6 illustrates the impact on concentration profiles of copper oxide concentration, chemical reaction parameter, endothermic–exothermic reaction parameter, and Schmidt number. Figure 6a shows the effect of copper oxide concentra-

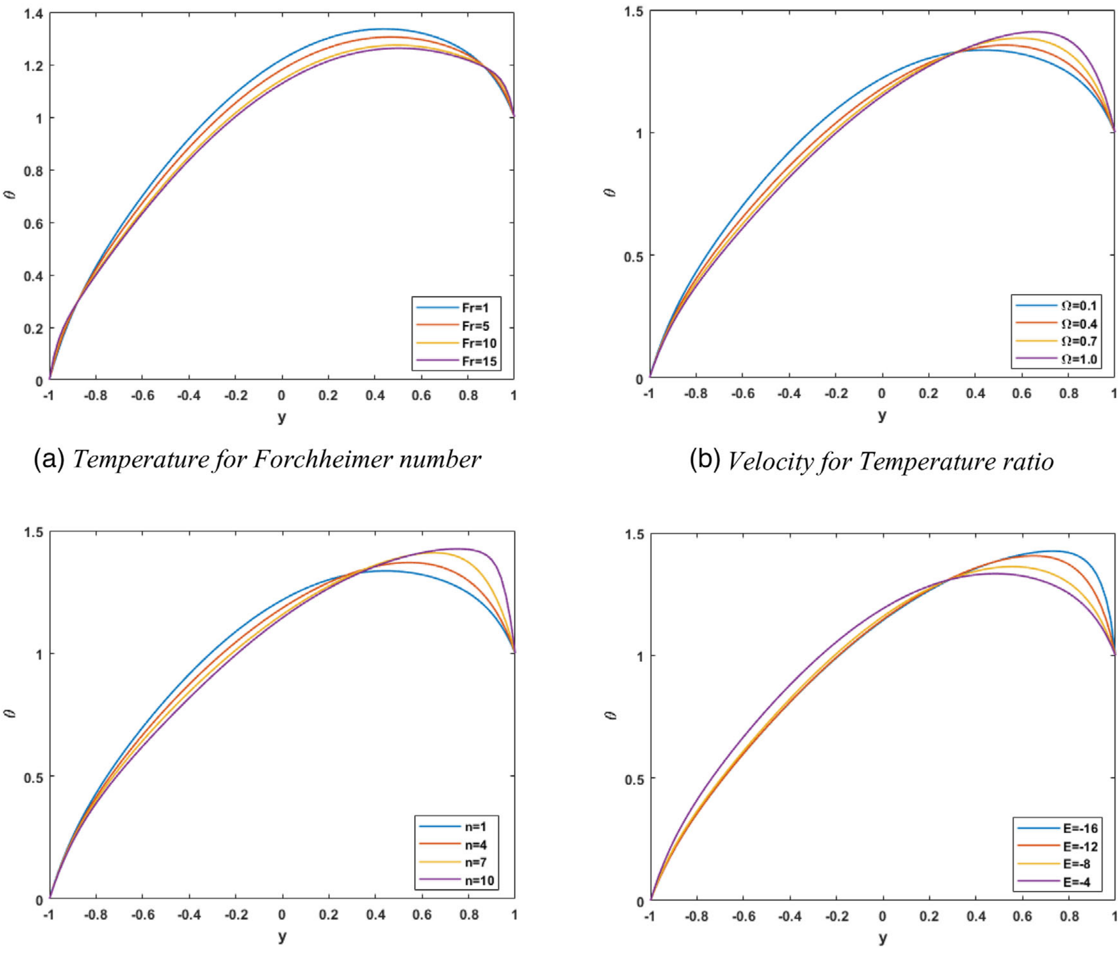

(a) *Temperature for Forchheimer number*

(b) *Velocity for Temperature ratio*

(c) *Velocity for fitting constant*

(d) *Velocity for Activation energy parameter*

FIGURE 5 (a) Temperature for Forchheimer number. (b) Velocity for temperature ratio. (c) Velocity for fitting constant. (d) Velocity for activation energy parameter.

tion on the concentration profiles. By increasing the concentration of copper oxide, the concentration of fluid increases. Physically, on increasing the nanoparticle concentration, the concentration increases are obvious. The fluid concentration is the sum of the nanoparticle concentrations. Figure 6b shows that the concentration increases with increasing the endothermic–exothermic parameter. The parameter value for an exothermic reaction is negative, and it is positive for an endothermic reaction. Nanoparticles absorb energy from their surroundings to surmount the activation energy barrier during an endothermic reaction. The ambient temperature decreases while the fluid temperature rises. Figure 6c depicts the effect of chemical reaction parameters on the fluid concentration. This shows that the concentration also increases with increasing parameter values. An incline in concentration behavior is observed for a growing chemical reaction's parameter value. It is believed that the expansion of the chemical reaction parameter near the surface of walls increases the concentration of the hybrid nanofluid and the thickness of the boundary layer, thereby enhancing the collision between fluid particles. Figure 5c shows the change in Schmidt number with the fluid concentration. As the Schmidt number increases, the concentration of hybrid nanofluids increases. Increasing the Schmidt number decreases the molecular diffusivity. The Schmidt number is one of the dimensionless numbers and is defined as the relationship between momentum and mass diffusivity. Consequently, as the Schmidt number increases, the hybrid nanofluid concentration rises.

5.4 | Electroosmosis profiles

The effect of zeta potential and electroosmotic number on the electroosmosis process is depicted in Figure 7. The effect of the electroosmotic number (K) on electroosmosis is depicted in Figure 7a. Upon increasing K, electroosmosis ini-

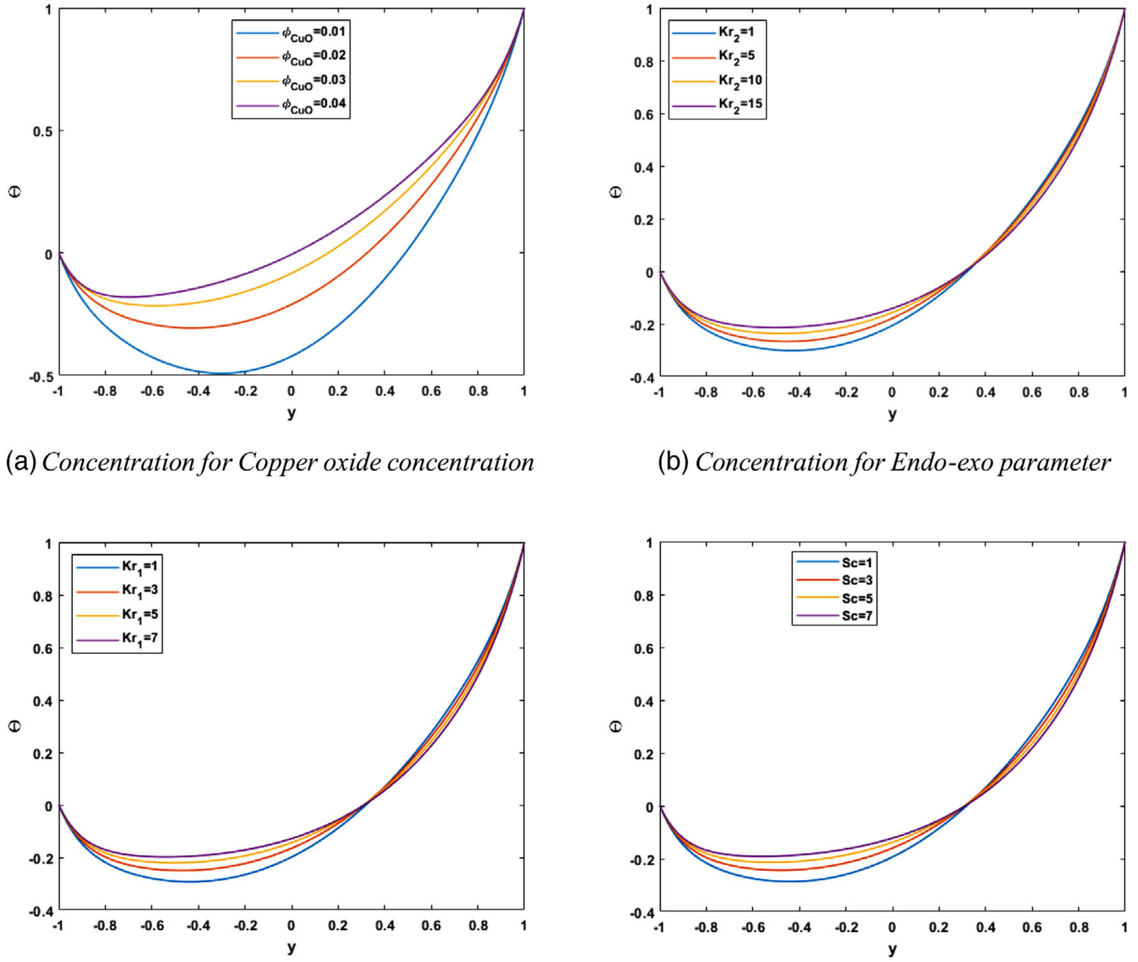

(a) *Concentration for Copper oxide concentration* (b) *Concentration for Endo-exo parameter*

(c) *Concentration for Chemical reaction parameter* (d) *Concentration for Schmidt number*

FIGURE 6 (a) Concentration for copper oxide concentration. (b) Concentration for endo-exo parameters. (c) Concentration for chemical reaction parameter. (d) Concentration for Schmidt number.

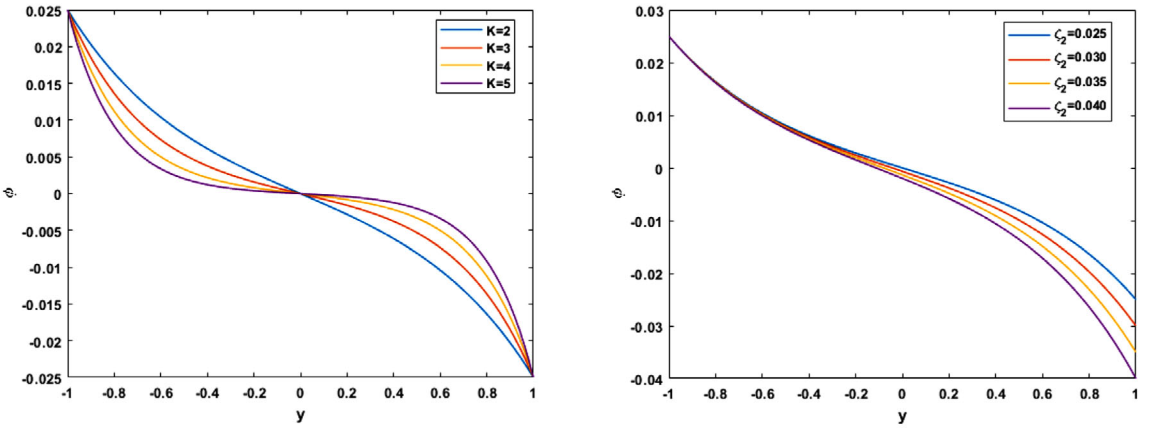

(a) *Electroosmosis for Electroosmotic parameter* (b) *Electroosmosis for Zeta potential*

FIGURE 7 (a) Electroosmosis for electroosmotic parameters. (b) Electroosmosis for Zeta potential.

tially decreased and then increased. This behavior is anticipated because an increase in Debye thickness induces a thin electric double layer, resulting in a significant increase in liquid flow at the epicenter of the pump. Figure 7b depicts the effect of the right wall's zeta potential on electroosmosis. It demonstrates that as the zeta potential increases, the electroosmosis process weakens. Mathematically, the zeta potentials are utilized in this model's boundary condition. Physically, the potential distribution is proportional to the electrical field intensity. The greater the zeta potential, the greater the concentration of ions adjacent to the channel wall, and the quicker the potential rises. Consequently, the electrical field intensity is confined to a thin layer close to the channel wall, decreasing as the zeta potential increases. When the zeta potential is sufficiently high, the electrical field strength at the interface dominates the thin layer.

5.5 | Velocity contours

Figure 8 represents the impact of the Darcy number, Forchheimer number, magnetic number, and solutal Grashof number on the velocity of the hybrid nanofluid. Figure 8a shows the effect of the Darcy number on the velocity. On increasing the Darcy number, the size of the boluses, the size of the annulus, and the gap between the layers increase. For $Da = 5, 10$, and a velocity value of 3, boluses are formed in the middle of bubbles. For $Da = 1$ and $Da = 10$, there is also a sufficient increase in the distance between the layers. Figure 8b depicts the effect of increasing the Forchheimer number. For $Fr = 1, 2$, and 3, the size of the boluses decreases. The size of the annulus remains constant for all Forchheimer number values. For $Fr = 2$ to $Fr = 3$, the bolus size is again increased. Figure 8c represents the effects of the changes in the magnetic field on the velocity. The bolus size first increases by making $Fr = 2$ from $Fr = 1$. Then, the bolus size decreases for the $Fr = 3$ value. On increasing Fr, there is a merging effect of annulus regions. For $Fr = 3$, there is almost a merging of the annulus. Figure 8d depicts the solutal Grashof number effect on the velocity. It shows a decline of the annulus region with increasing Gc. The gap between the waves remains constant for all Gc values. Higher values of boluses are formed for $Gc = 5$ from $Gc = 3$.

6 | VELOCITY SURFACE PLOTS

Figure 9 shows the effect of the Forchheimer number and the time-average flow rate parameter. Figure 9a shows that the velocity decreases when enhancing the values of the Forchheimer number. For enhanced values of the Forchheimer number, the highly porous nature of the microchannel increases. The figure also shows that the layers' left and right sides meet at the plot's upper part. Figure 9b illustrates the impact of the time-average flow rate parameter on fluid velocity. It shows that the velocity increases for enhanced values of the time-average flow rate parameter. The time-average flow rate parameter is used in the boundary conditions of the flow's governing equations.

6.1 | Temperature surface plots

Figure 10 gives a glimpse of the temperature surface plots for the heat source and Darcy number. Figure 10a shows that the temperature increases with higher values of the heat source parameter. As the heat source strengthens, the amount of heat energy in the flow system and the temperature increase. Figure 10b represents the enhancement of the Darcy number on the temperature. The figure shows that the temperature increases for enhanced values of the Darcy number. On boosting up the Darcy number, the porous nature of the microchannel increases. The nanoparticles experience more resistance to movement. This increases the frictional heating and, hence, the temperature.

6.2 | Concentration surface plots

Figure 11 shows the effect of the thermophoretic parameter and the Brownian motion parameter on the fluid concentration. Figure 11a depicts the thermophoresis parameter effect on the fluid. It is demonstrated that greater thermophoretic parameter values result in increased concentration. This is because particles close to the channel walls generate a ther-

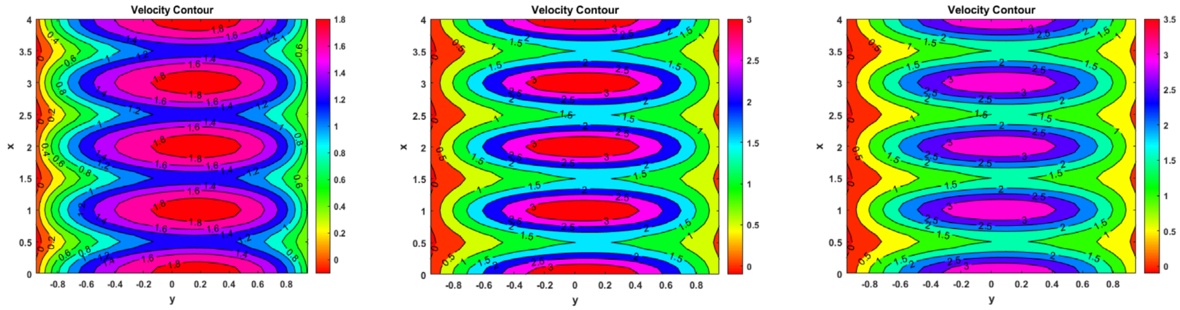

(a) *Velocity contours for Darcy number (Da = 1, 5, 10)*

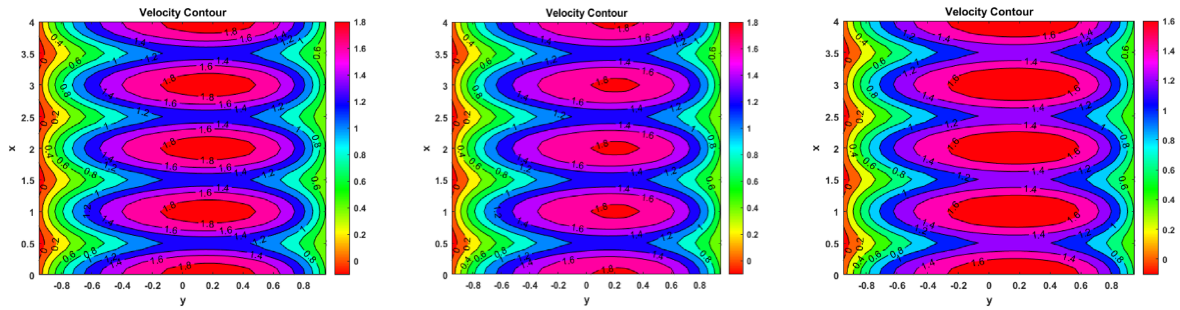

(b) *Velocity contours for Forchheimer number (Fr = 1, 2, 3)*

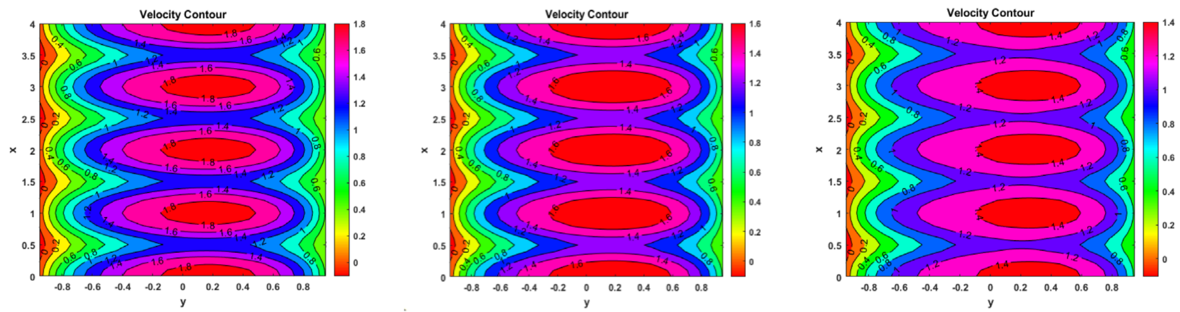

(c) *Velocity contours for Magnetic number (M = 1, 5, 10)*

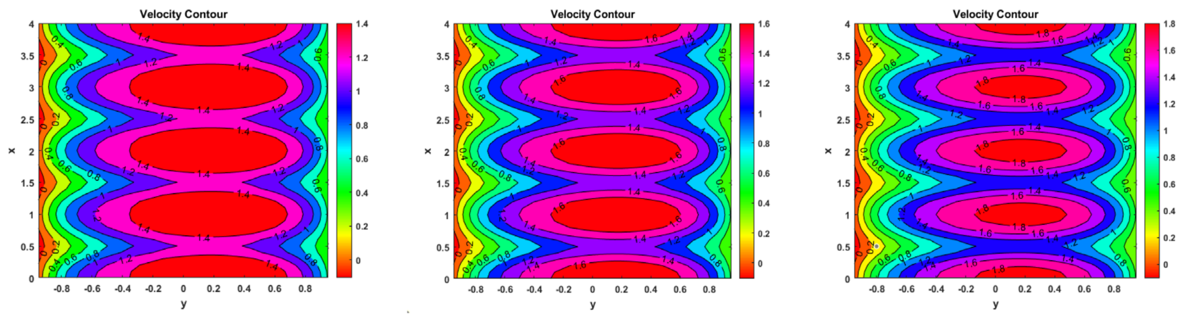

(d) *Velocity contours for Solutal Grashof number (Gc = 1, 3, 5)*

FIGURE 8 (a) Velocity contours for Darcy number ($Da = 1, 5, 10$). (b) Velocity contours for Forchheimer number ($Fr = 1, 2, 3$). (c) Velocity contours for magnetic number ($M = 1, 5, 10$). (d) Velocity contours for Solutal Grashof number ($Gc = 1, 3, 5$).

mophoretic force that assists particle disintegration away from the fluid regime, thereby increasing concentration and boundary layer thicknesses. The impact of the Brownian parameter on concentration is seen in Figure 11b. Particles in a fluid exhibit Brownian motion, or random motion, because of the fast-moving atoms or molecules of the base fluid. Particle size and Brownian motion are connected, and agglomerates of small particles are common. Because Brownian motion is so weak for heavy particles, their values will be near the bottom of the range.

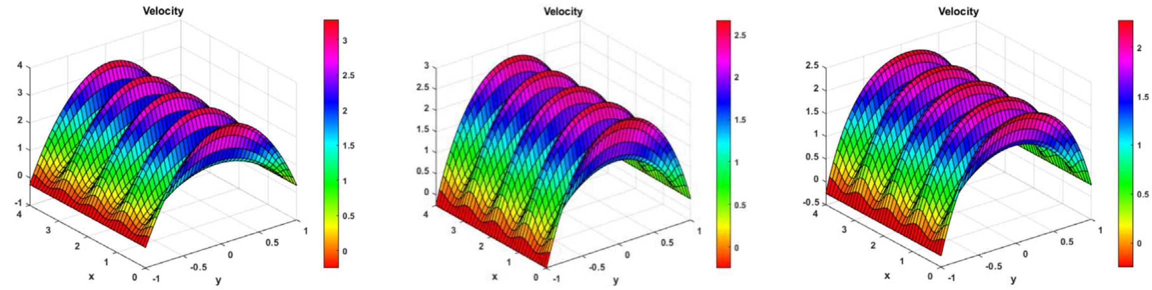

(a) *Velocity surface plots for Forchheimer number (Fr = 0.05, 2.5, 5)*

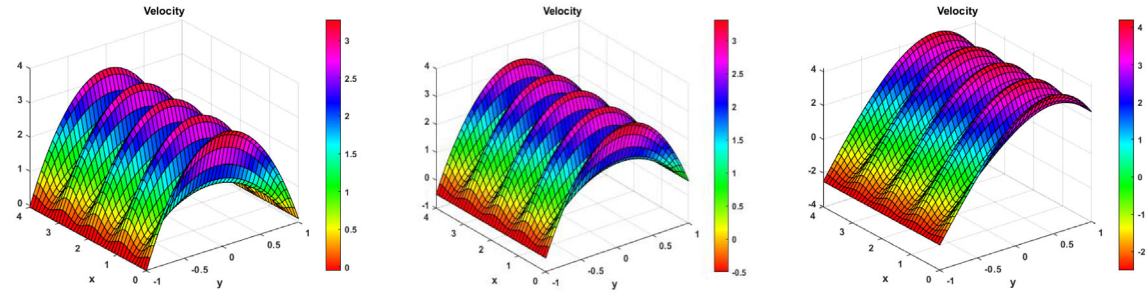

(b) *Velocity surface plots for Time-average flow rate (F = 0.01, 0.1, 0.5)*

FIGURE 9 (a) Velocity surface plots for Forchheimer number ($Fr = 0.05, 2.5, 5$). (b) Velocity surface plots for time-average flow rate ($F = 0.01, 0.1, 0.5$).

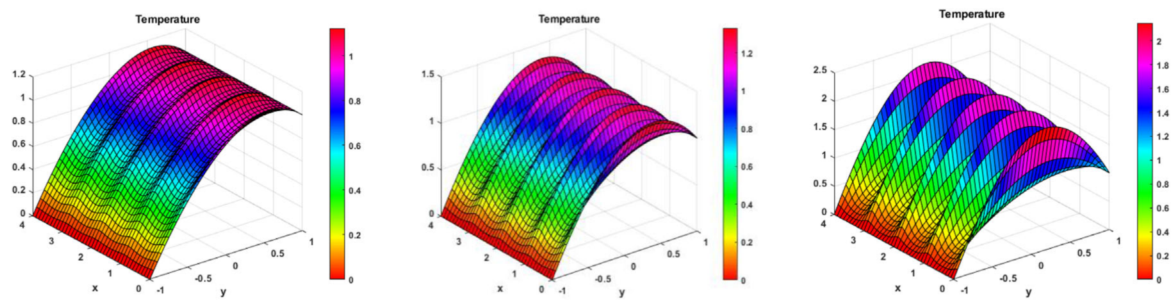

(a) *Velocity surface plots for Forchheimer number (Q = 1, 2.5, 5)*

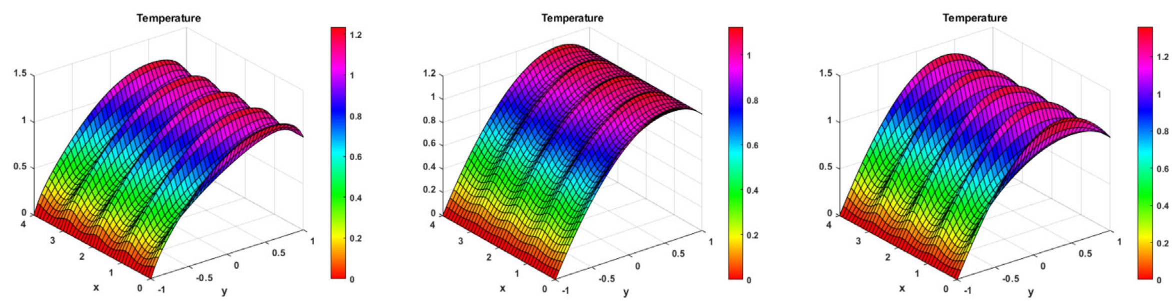

(b) *Velocity surface plots for Forchheimer number (Da = 0.01, 0.1, 1)*

FIGURE 10 (a) Velocity surface plots for Forchheimer number ($Q = 1, 2.5, 5$). (b) Velocity surface plots for Forchheimer number ($Da = 0.01, 0.1, 1$).

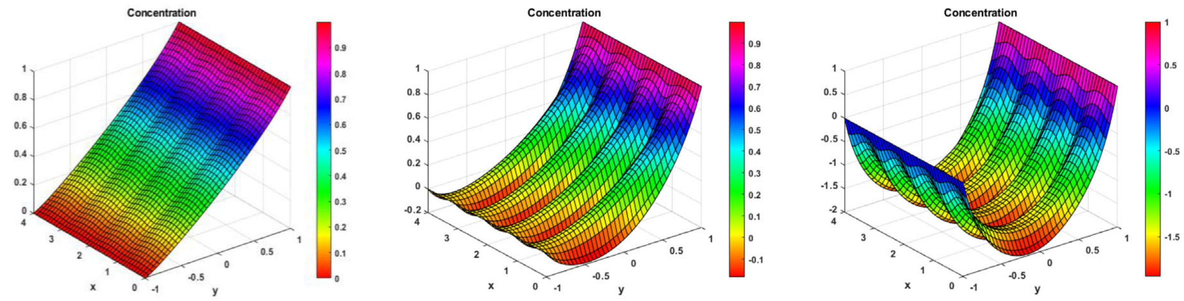

(a) *Concentration surface plots for Thermophoresis parameter (Nt = 0.1, 0.5, 1)*

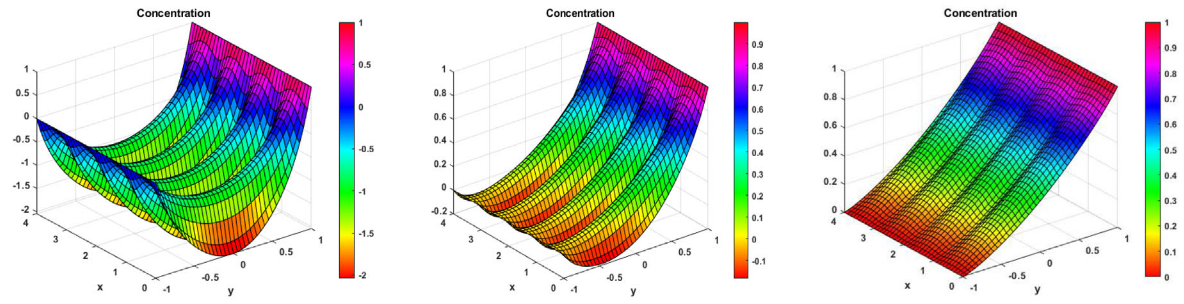

(b) *Concentration surface plots for Brownian motion parameter (Nb = 0.1, 0.5, 1)*

FIGURE 11 (a) Concentration surface plots for thermophoresis parameters ($Nt = 0.1, 0.5, 1$). (b) Concentration surface plots for Brownian motion parameter ($Nb = 0.1, 0.5, 1$).

6.3 | Electroosmosis surface plots

Figure 12a gives information about the changing effect of the electroosmosis parameter on the electroosmosis surface waves. The plot shows that for enhanced parameter values, the electroosmosis decreases for the first half and then increases for the second half. The change happens at $y = 0$. This behavior is anticipated because an increase in Debye thickness induces a thin electric double layer, resulting in a significant increase in liquid flow at the epicenter of the pump.

6.4 | Physical significance quantities

Figure 13 depicts the effect on skin friction coefficient, heat transfer rate, mass transfer rate, entropy generation, and Bejan number for various flow parameters. Figure 13a shows the effect of Forchheimer and solutal Grashof numbers on the skin friction coefficient. For larger values of the Forchheimer number, the skin friction increases. For enhanced values

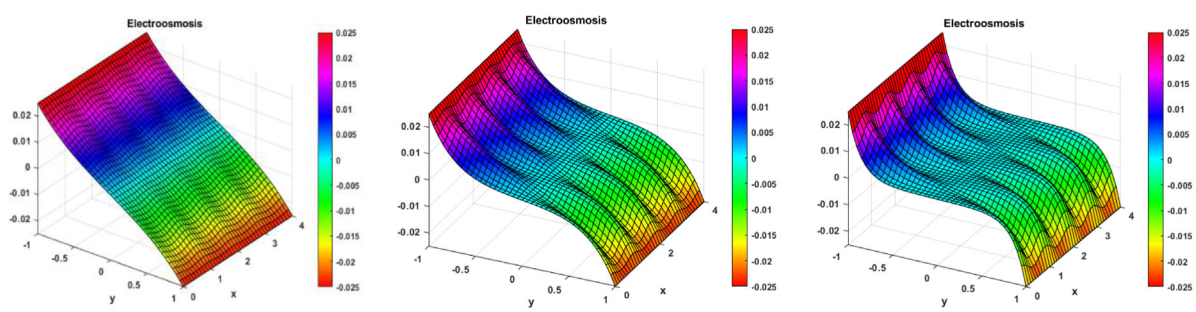

(a) *Electroosmosis surface plots for Electroosmosis parameter (K = 1, 5, 10)*

FIGURE 12 (a) Electroosmosis surface plots for electroosmosis parameters ($K = 1, 5, 10$).

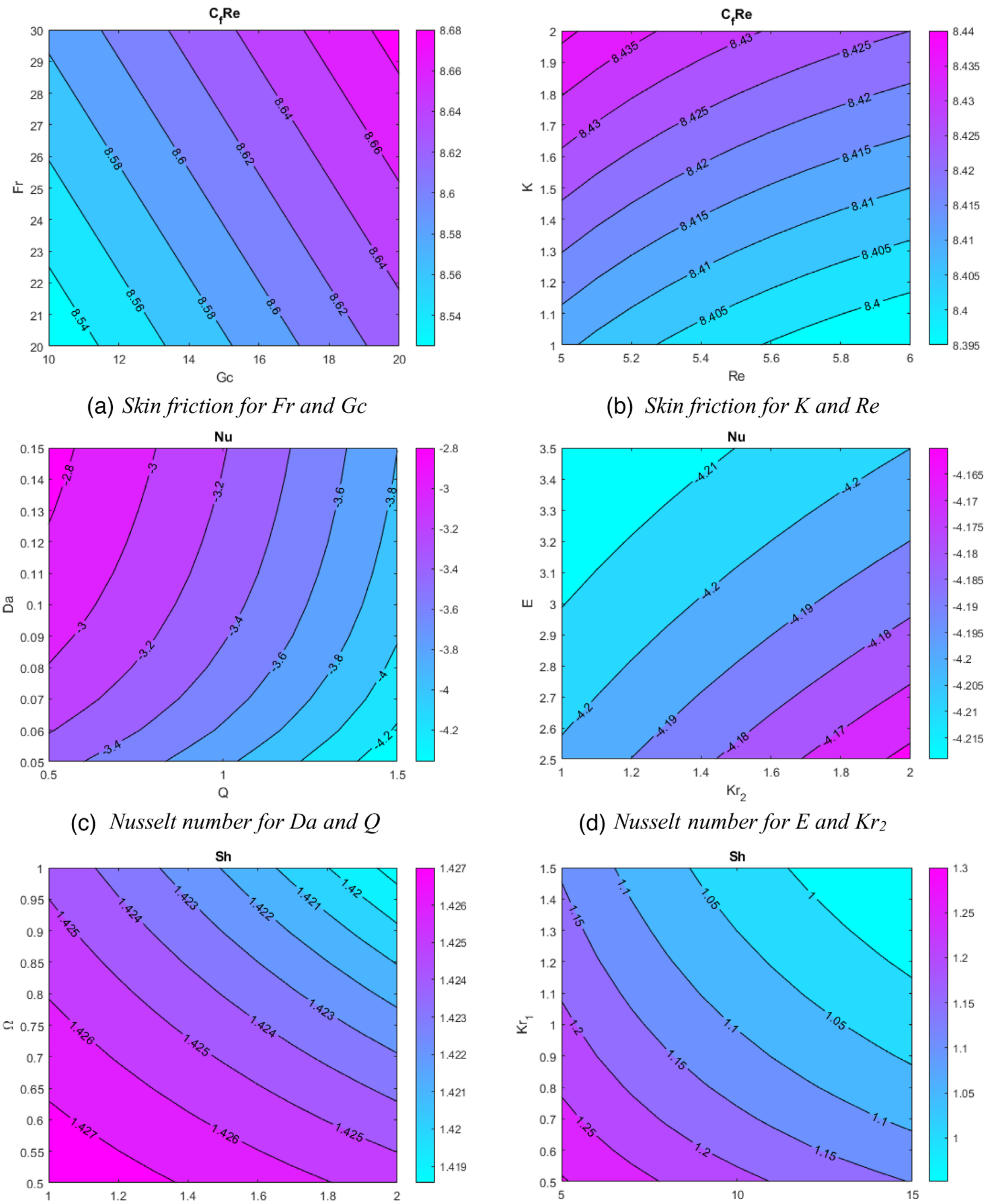

(a) *Skin friction for Fr and Gc*

(b) *Skin friction for K and Re*

(c) *Nusselt number for Da and Q*

(d) *Nusselt number for E and Kr_2*

(e) *Sherwood number for Ω and n*

(f) *Sherwood number for Kr_1 and Sc*

FIGURE 13 (a) Skin friction for Fr and Gc. (b) Skin friction for K and Re. (c) Nusselt number for Da and Q. (d) Nusselt number for E and Kr_2. (e) Sherwood number for $\boldsymbol{\Omega}$ and n. (f) Sherwood number for Kr_1 and Sc. (g) Entropy generation for Nt and Nb. (h) Entropy generation for E and Kr_2. (i) Bejan number for Nt and Nb. (j) Bejan number for E and Kr_2.

of the solutal Grashof number, the skin friction coefficient boosts up. Figure 13b represents the effect of the electroosmosis parameter and Reynolds number on the skin friction coefficient. The figure shows that the skin friction coefficient increases with the enhanced electroosmosis parameter. On increasing the Reynolds number, the coefficient decreases. Figure 13c depicts the effect of the Darcy number and heat source parameters on the heat transfer rate, or the Nusselt

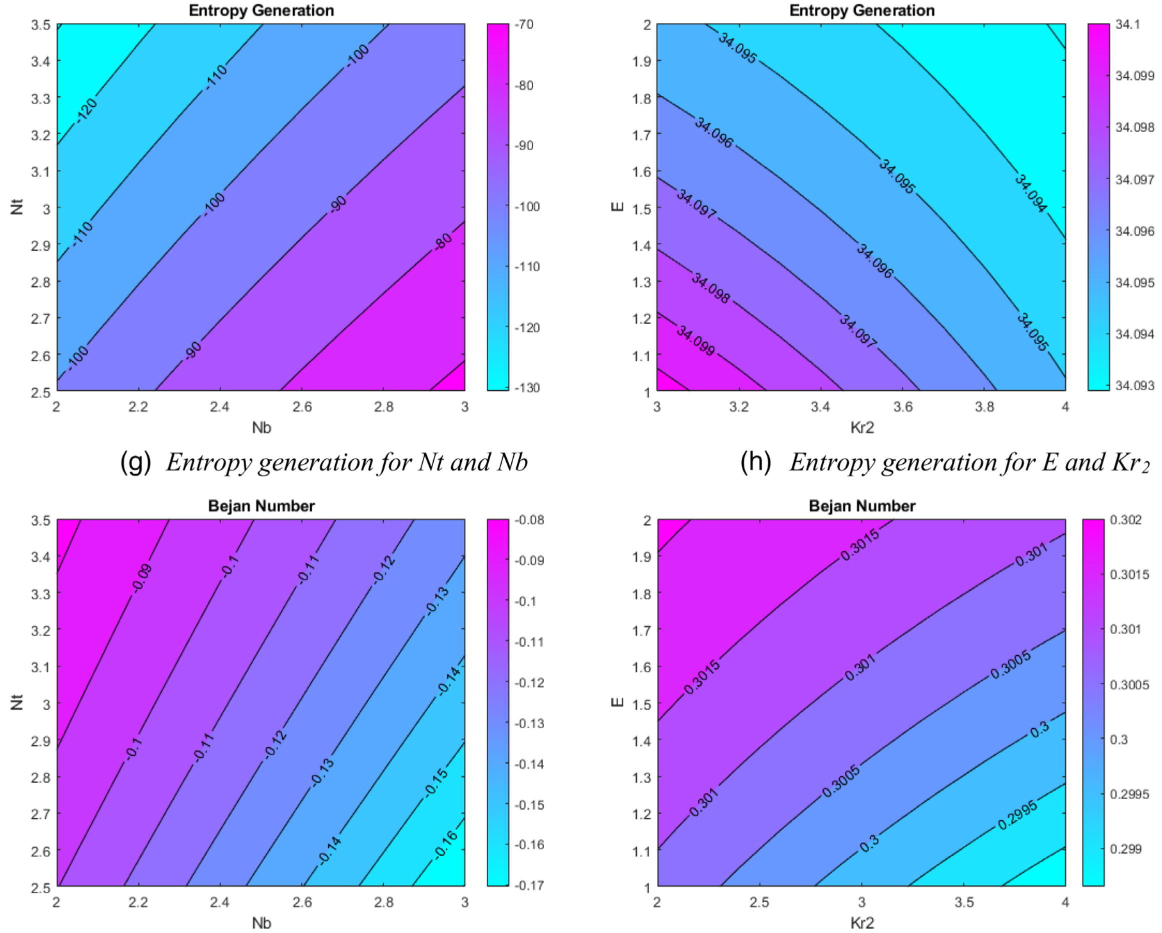

(g) *Entropy generation for Nt and Nb* (h) *Entropy generation for E and Kr_2*

(i) *Bejan number for Nt and Nb* (j) *Bejan number for E and Kr_2*

FIGURE 13 (Continued)

number. The figure shows that for enhanced values of the Darcy number, the Nusselt number decreases in the negative direction. On boosting the heat source parameter, the Nusselt number increases in the negative direction.

Figure 13d shows the effect of the activation energy and endothermic–exothermic reaction parameters on the Nusselt number. The figure shows that the Nusselt number increases in the negative direction when increasing the activation energy parameter. For stronger values of the endothermic–exothermic reaction parameter, the Nusselt number decreases negatively. Figure 13e represents the impact of the temperature ratio parameter and the temperature fitting constant on the mass transfer rate, or the Sherwood number. The figure shows that for enhanced values of the temperature ratio, the Sherwood number decreases. On increasing the fitting constant parameter, the Sherwood number again lowers. Figure 13f shows the changes in the chemical reaction parameter and Schmidt number on the Sherwood number. The figure shows that for enhanced chemical reaction parameters, the Sherwood number decreases. The figure also shows that by boosting the Schmidt number, the Sherwood number weakens. Figure 13g depicts the thermophoresis and Brownian motion parameters of the entropy generated in the fluid. The figure shows that when the thermophoresis parameter is increased, the entropy generation increases in the negative direction. For boosted values of the Brownian motion parameter, the entropy decreases in the negative direction. Figure 13h represents the impact on the entropy of the activation energy parameter and the endothermic–exothermic chemical reaction. The figure shows that increasing the activation energy parameter makes the fluid's generated entropy weak. The entropy generated is reduced for enhanced values of the endothermic–exothermic parameter. Figure 13i displays the impact on the Bejan number of changing thermophoresis and Brownian motion parameter values. The figure shows that for increasing values of the thermophoresis parameter, the Bejan number decreases in the negative direction. For larger values of the Brownian parameter, the Bejan number increases on the negative side. Figure 13j gives information on activation energy and endothermic–exothermic reaction parameters. The figure shows that the Bejan number increases with enhanced activation energy. Then, the Bejan number decreases for a larger endothermic–exothermic parameter.

7 | ARTIFICIAL NEURAL NETWORK ANALYSIS

After getting the solutions of the ODEs (23–26), the axial velocity, temperature, concentration, and electroosmosis values are used to train an artificial neural network using the BRBP algorithm. This trained network consists of data points obtained from the various values of dimensionless numbers. The obtained networks are graphically analyzed using training state, performance, fit, regression, and error histogram plots. From this analysis, the reader can get a glimpse of how to set the flow parameter values to obtain the desired network. The accuracy of the trained model is analyzed using the regression plots. The regression coefficient, R is the representative of the accuracy. For a perfect model, $R = 1$. Any other R value shows significant deviations in the model. The current section discussed the accuracy of the current models based on the R values.

7.1 | Training state plots

Figure 14 shows the training state plots for the BRBP algorithm trained for various values of magnetic field number, Forchheimer number, activation energy parameter, and solutal Grashof number. Figure 14a depicts the training plot for the magnetic parameter. The number of epochs used for training decreases by increasing the magnetic number. The gradient value rises, and mu, the learning rate, decreases by 100 times. The numerical parameters increases. The sum of the squared parameters boosts up for a sufficient margin. The validation failure checks remain the same at 0. Figure 14b shows the training plot for the Forchheimer number. It shows that increasing the Forchheimer values increases the number of epochs used for training the plot. The learning rate, mu, increases by 10 times. The numerical parameters increase a bit. The sum of the squared parameters decreases, and the validation checks remain constant. There is no validation failure seen throughout the model training. Figure 14c represents the training state plots for the activation energy parameter. The figure shows that the epoch used for training the model increased with increasing parameter values. The learning rate, mu, increased by 10 times. The numerical parameter values decreased by a smaller magnitude. The sum of the squared parameters decreased by half. There are no validation failures seen again. Figure 14d depicts the effect of the solutal Grashof number on the model's training. For larger values of the solutal Grashof number, the number of epochs increased drastically. From 12, they reached 152. The learning rate decreased by 10 times. The numerical parameters increased a bit. The sum of the squared parameters increased by around 2000. Again, the validation check value remained constant, that is, 0.

7.2 | Performance plots

Figure 15 shows the performance plot for the ANN model training for magnetic numbers, Forchheimer numbers, activation energy parameters, and solutal Grashof numbers. The purpose of figure 14a is to show how, on changing the magnetic strength, the model's performance varied. The training error decreased continuously for every epoch with $M = 1$. Then, for $M = 5$, the training error decreased until the 20th epoch and became constant. The same can be seen for testing errors. For smaller magnetic numbers, the testing error saw a good drop until the 10th epoch. Figure 15b shows the effect of the Forchheimer number on the model's performance. The figure tells us that the training and testing errors stagnated for the lower Forchheimer number after the 10th epoch. For larger Forchheimer values, both errors decreased first drastically, then kept on dropping. The best-fit line corresponds to the errors of the last epoch for higher Forchheimer values. Figure 15c represents the impact of the activation energy parameter on the algorithm's performance. The training and testing errors could not get a constant value until the stopping condition was met for both values of the parameter. For smaller parameter values, the testing error decreased first, then increased again after the 150th epoch. However, the training error follows the same decreasing effect until the end. Figure 15d illustrates the changes in solutal Grashof number on the training plots. The plot shows that for smaller solutal Grashof number values, there is a wavy nature to the errors for the epochs. The training error reached the minimum error at the last epoch. The errors were almost stable for the larger solutal Grashof number for the first 10 epochs. Still, the decreasing effect continued.

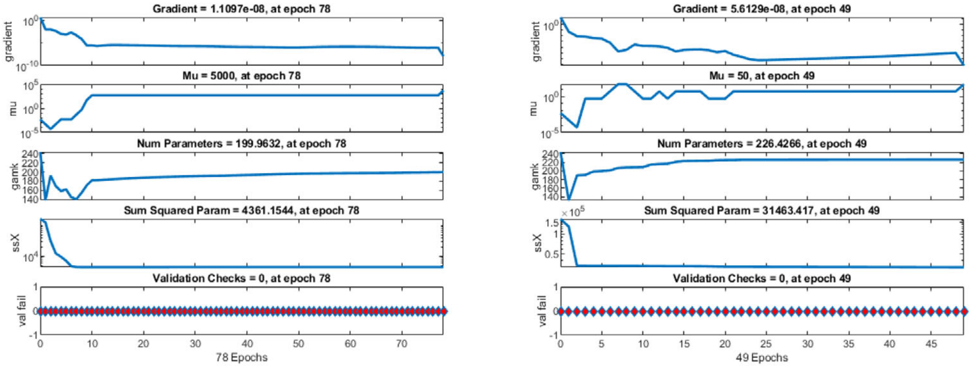

(a) *Training state plots for Magnetic parameter (M = 1, 5)*

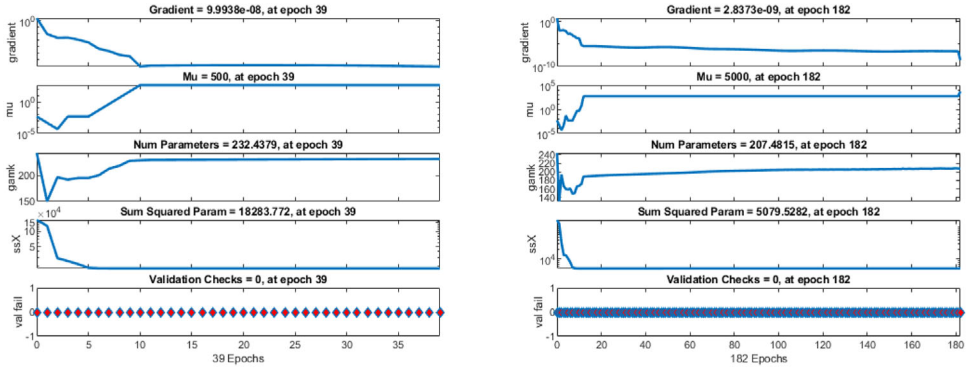

(b) *Training state plots for Forchheimer number (Fr = 1, 5)*

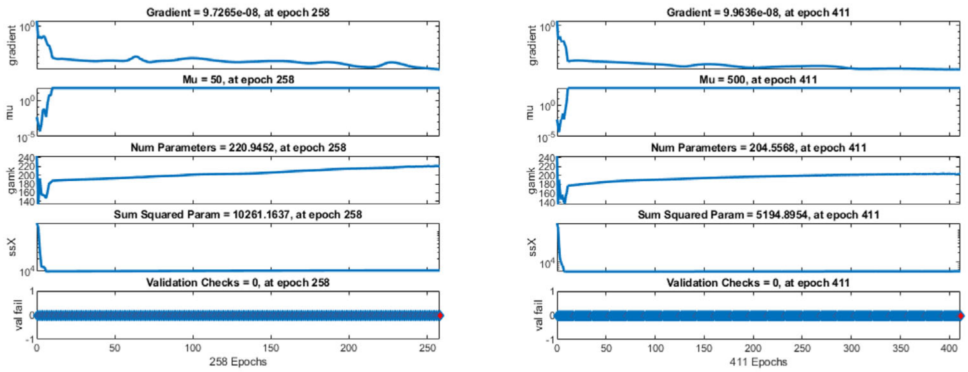

(c) *Training state plots for Activation energy parameter (E = 5, 10)*

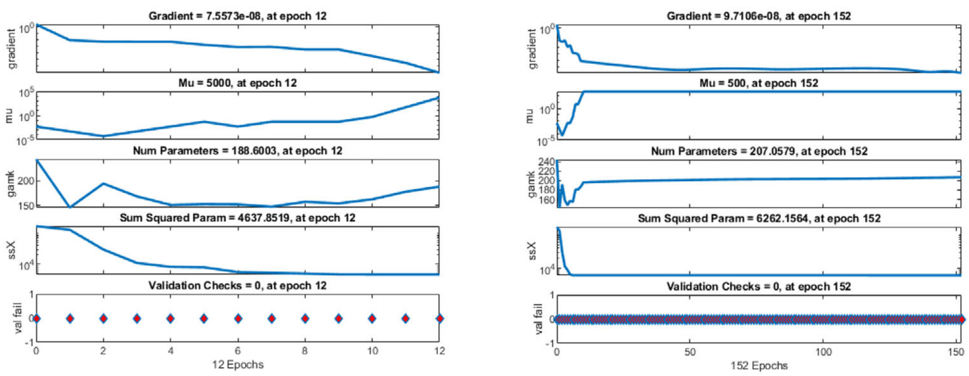

(d) *Training state plots for Solutal Grashof number (Gc = 1, 3)*

FIGURE 14 (a) Training state plots for magnetic parameters ($M = 1, 5$). (b) Training state plots for Forchheimer numbers ($Fr = 1, 5$). (c) Training state plots for activation energy parameters ($E = 5, 10$). (d) Training state plots for solutal Grashof number ($Gc = 1, 3$).

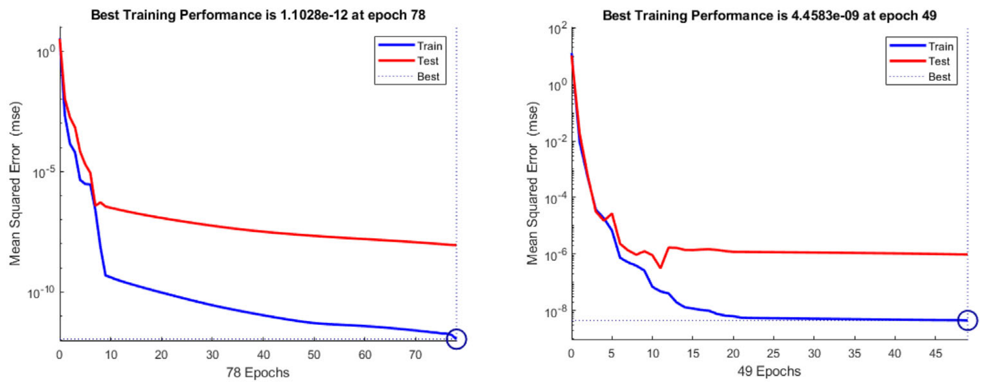

(a) *Performance plots for Magnetic parameter (M = 1, 5)*

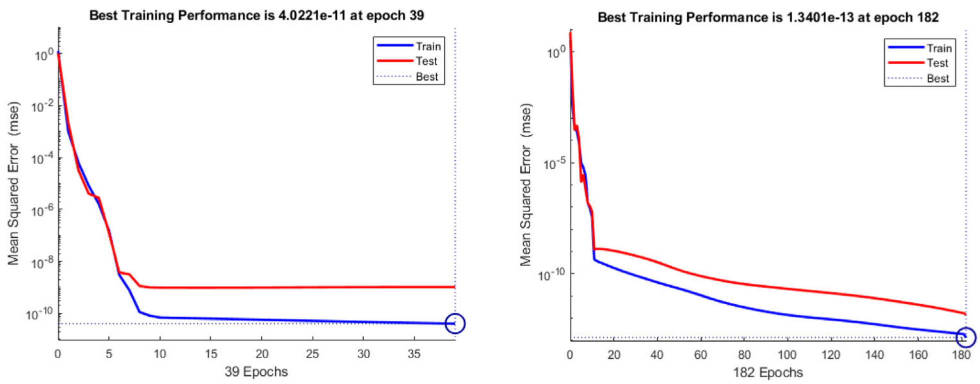

(b) *Performance plots for Forchheimer number (Fr = 1, 5)*

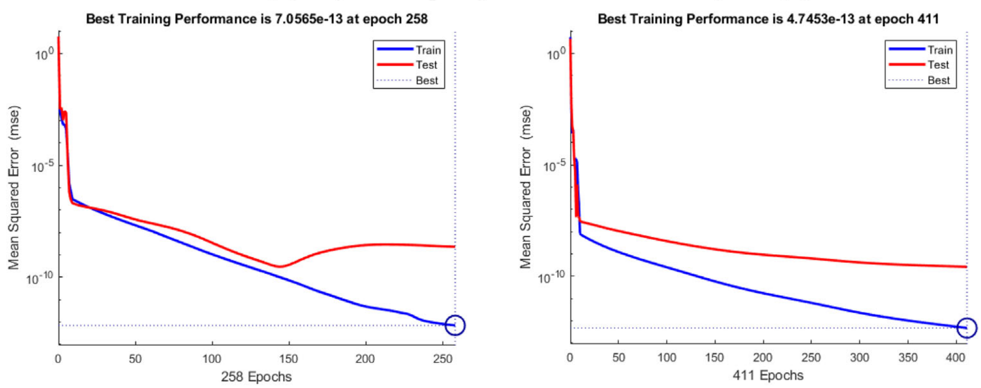

(c) *Performance plots for Activation energy parameter (E = 5, 10)*

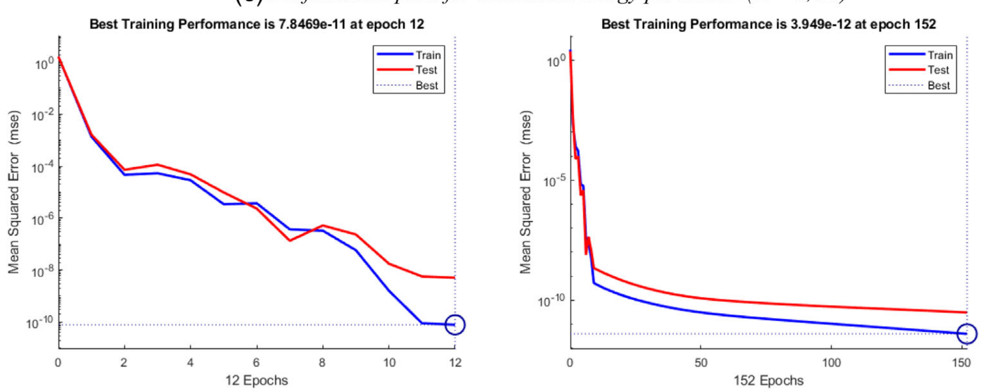

(d) *Performance plots for Solutal Grashof number (Gc = 1, 3)*

FIGURE 15 (a) Performance plots for magnetic parameters ($M = 1, 5$). (b) Performance plots for Forchheimer number ($Fr = 1, 5$). (c) Performance plots for activation energy parameter ($E = 5, 10$). (d) Performance plots for solutal Grashof number ($Gc = 1, 3$).

7.3 | Error histogram plots

Figure 16 shows the error histograms for magnetic numbers, Forchheimer numbers, activation energy parameters, and solutal Grashof numbers. Figure 16a represents the effect of magnetic field numbers on the error histograms. For lower magnetic strengths, all the instances fall into the zero-error bin. This can be considered the ideal state of the model. The zero line corresponds to the zero error. This line falls into the zero-error bin. For higher magnetic number values, some nonzero-error bins are formed around the main bin.

The number of testing dataset instances also decreased for the zero-error bin. Figure 16b represents the Forchheimer number effect on the model's error histograms. The figure shows that for enhanced values of the Forchheimer number, there are decreases in the zero-error bin instances. For lower Forchheimer values, the zero-error bin lines up between 250 and 300. This comes to 200–250 if you increase the Forchheimer values. Some higher error bins are also formed on the right of the zero line. Figure 16c shows the activation energy parameter and the model's performance plot. The figure reveals that the model reached an ideal lower activation energy parameter condition and gave perfect results. On enhancing the activation energy parameter, one nonzero-error bin forms before the zero line. Figure 16d represents the effect of the solutal Grashof number on the performance plot. It can be observed in the figure that for raised values of the solutal Grashof number, the model performance decreases heavily. For the lower solutal Grashof number, there are around 340 zero-error instances. These come to around 180 instances. There are also many instances to the left of the zero line.

7.4 | Regression plots

Figure 17 illustrates the regression plot for the BRBP algorithm for magnetic number, Forchheimer number, activation energy parameter, and solutal Grashof number. Figure 17a reveals the magnetic field number effect on the regression testing of the obtained model. The figure shows that the regression coefficient remained constant, that is, 1 for both values of the magnetic number. However, it can be seen that a greater number of data points can be seen on the upper end of the regression line for the lower magnetic field parameter. The points are evenly distributed for higher magnetic values. Figure 17b depicts the effect of the Forchheimer number. Again, the regression constant remained the same for both values of the Forchheimer number. However, a change in the constants of the regression equations can be seen.

The equation constants increased by a unit on increasing the Forchheimer number. Plot 17c represents the effect of the activation energy parameter on the mode's regression plot. Again, there is not much change in the enhanced activation energy parameter. One unit difference exists in the equation's constant for testing data, training data, and all datasets. Now, Figure 17d reveals how the solutal Grashof number changes the regression plots. The regression coefficient remained constant for the enhanced solutal Grashof number, indicating that the model again predicted all correct values. A minute difference in the dataset distribution can be seen for all three datasets.

7.5 | Fit plots

Figure 18 illustrates the fit plots of the model again for the magnetic number, Forchheimer number, activation energy parameter, and solutal Grashof number. Figure 18a shows the fit plot for the magnetic number. For enhanced values of magnetic numbers, there is an upward shift in the targets and outputs. The error remains the same and comes mostly from the starting pointetic number, Forchheimer number, activation energy parameter, and solutal Grashof number. Figure 18a shows the fit plot for the magnetic number. For enhanced values of magnetic numbers, there is an upward shift in the targets and outputs. The error remains the same and comes mostly from the starting point. All the data are in accordance with the best-fit line. Figure 18b shows the fitting state of the model and the Forchheimer number. Both of these curves show almost identical behavior. All the output and target values revolve around the zero line itself. In the case of errors, there is a significant number of errors in the case of lower Forchheimer. It shows errors at the start as well as at the end. Both microchannel walls can see the errors. For higher Forchheimer numbers, there are error values only for smaller y-values. The plot in Figure 18c reveals the activation energy parameter effect on the fit plot. Error-wise, there are a greater number of error values in the case of a higher activation energy parameter. There is no error behavior seen for $y = 0$ values. There are fewer error instances for lower activation energy parameters, but the magnitude of error is very high

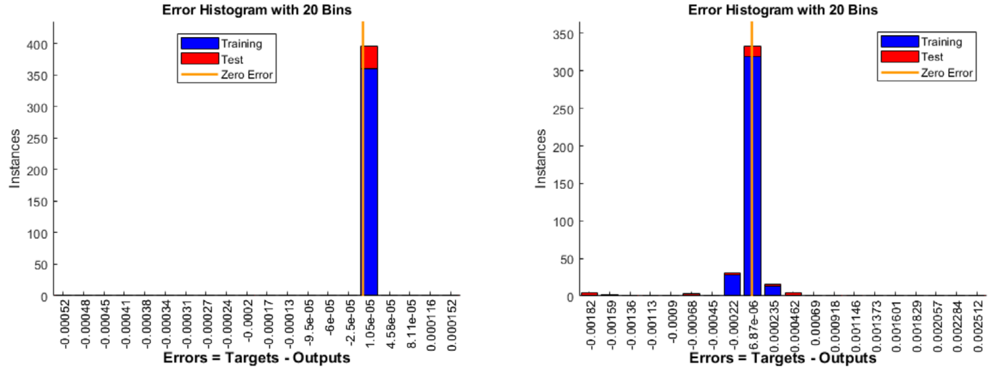

(a) *Error histogram plots for Magnetic parameter (M = 1, 5)*

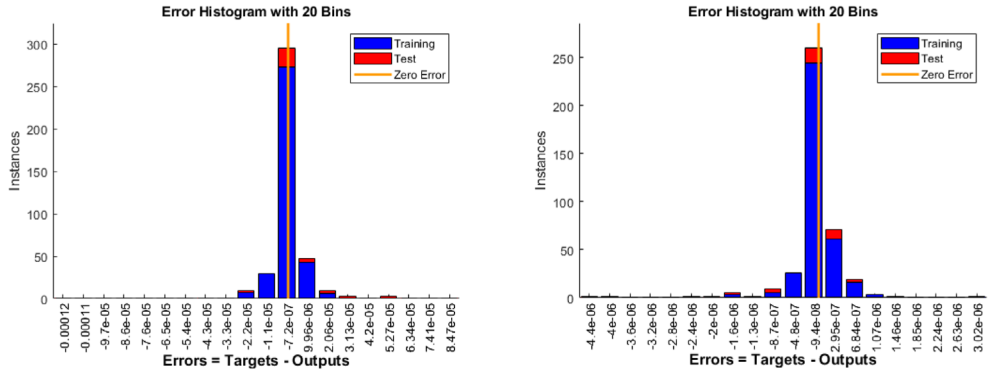

(b) *Error histogram plots for Forchheimer number (Fr = 1, 5)*

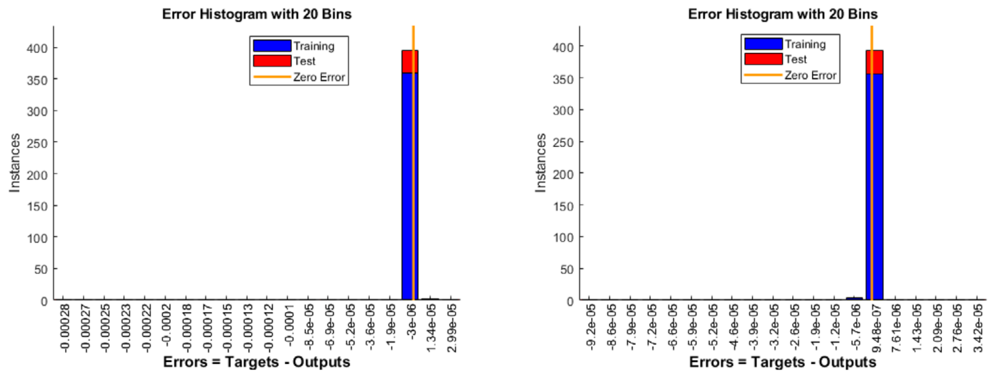

(c) *Error histogram plots for Activation energy parameter (E = 5, 10)*

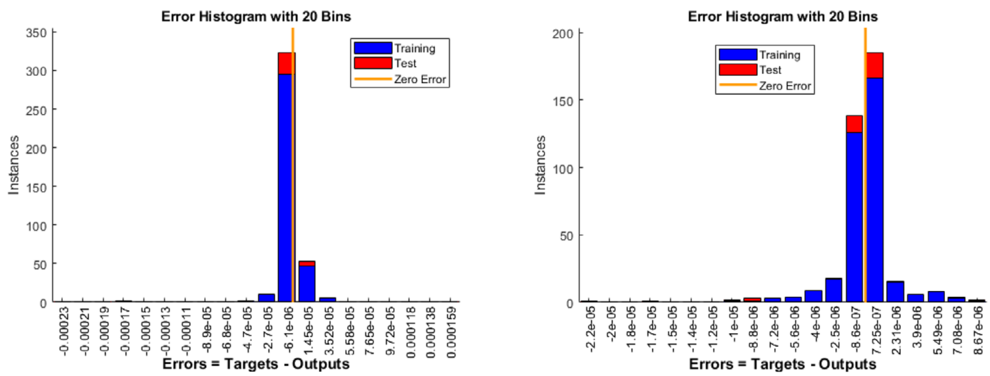

(d) *Error histogram plots for Solutal Grashof number (Gc = 1, 3)*

FIGURE 16 (a) Error histogram plots for magnetic parameters ($M = 1, 5$). (b) Error histogram plots for Forchheimer number ($Fr = 1, 5$). (c) Error histogram plots for activation energy parameter ($E = 5, 10$). (d) Error histogram plots for solutal Grashof number ($Gc = 1, 3$).

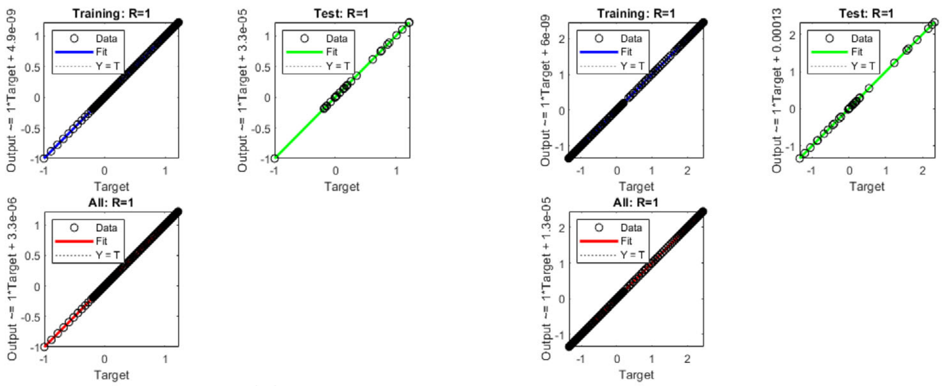

(a) *Regression plots for Magnetic parameter (M = 1, 5)*

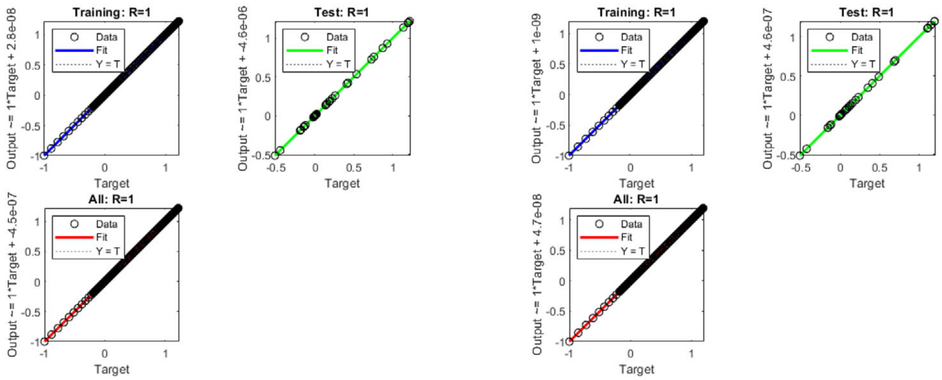

(b) *Regression plots for Forchheimer number (Fr = 1, 5)*

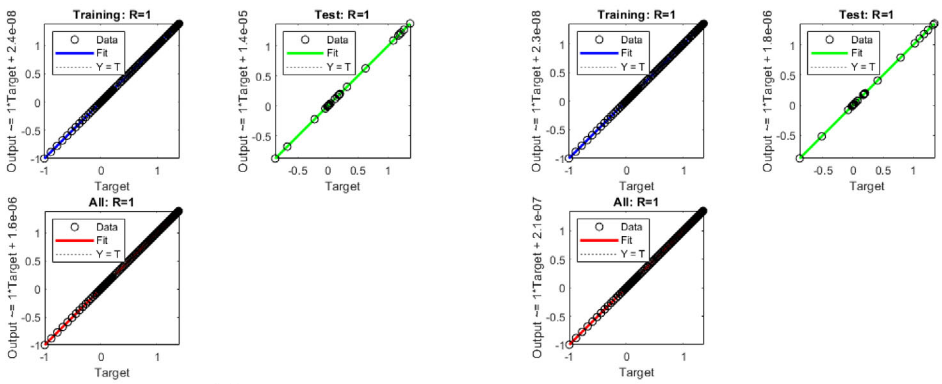

(c) *Regression plots for Activation energy parameter (E = 5, 10)*

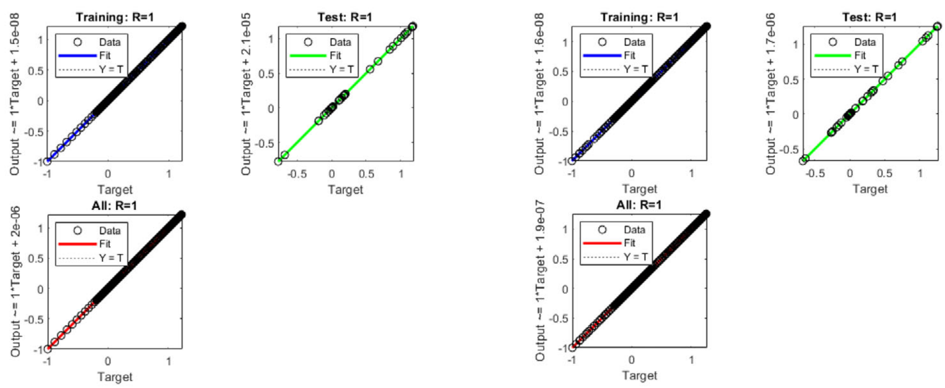

(d) *Regression plots for Solutal Grashof number (Gc = 1, 3)*

FIGURE 17 (a) Regression plots for magnetic parameters ($M = 1, 5$). (b) Regression plots for Forchheimer number ($Fr = 1, 5$). (c) Regression plots for activation energy parameter ($E = 5, 10$). (d) Regression plots for solutal Grashof number ($Gc = 1, 3$).

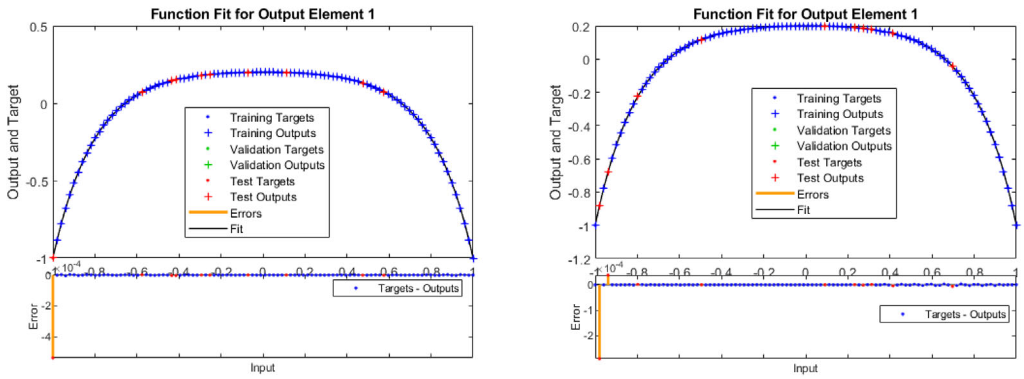

(a) *Fit plots for Magnetic parameter (M = 1, 5)*

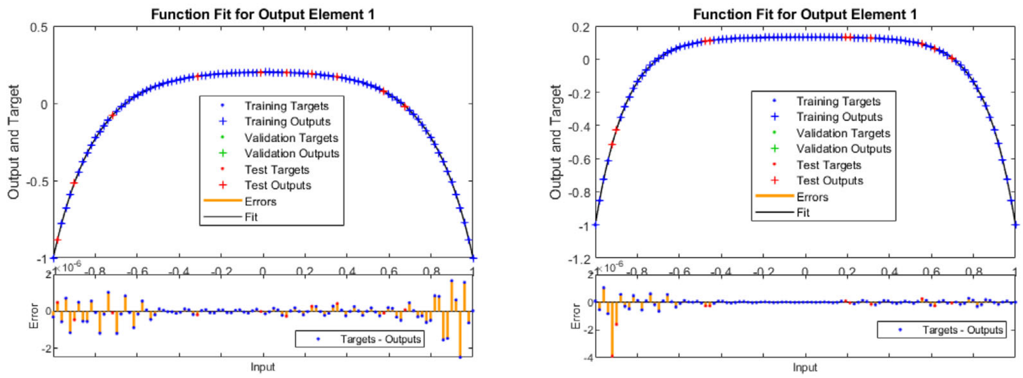

(b) *Fit plots for Forchheimer number (Fr = 1, 5)*

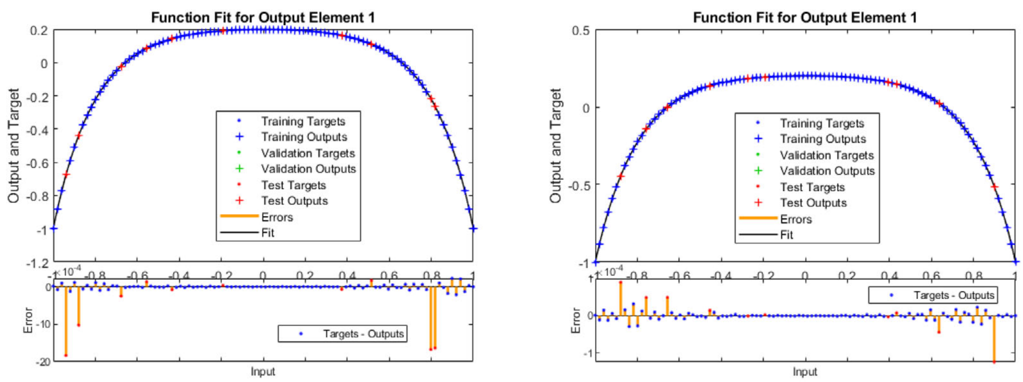

(c) *Fit plots for Activation energy parameter (E = 5, 10)*

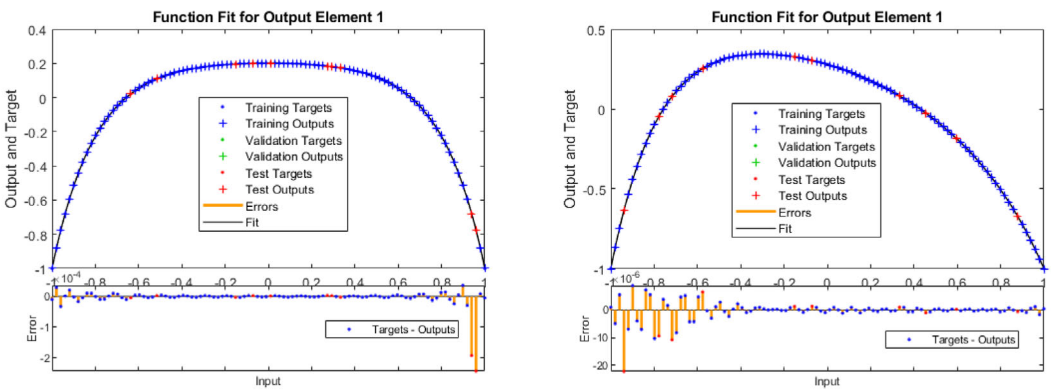

(d) *Fit plots for Solutal Grashof number (Gc = 1, 3)*

FIGURE 18 (a) Fit plots for magnetic parameter ($M = 1, 5$). (b) Fit plots for Forchheimer number ($Fr = 1, 5$). (c) Fit plots for activation energy parameters ($E = 5, 10$). (d) Fit plots for solutal Grashof number ($Gc = 1, 3$).

for lower and higher y-values. Figure 18d is for the sole Grashof number impact on the models' fit plot. It reveals that for lower solutal Grashof numbers, there are almost no errors for lower y-values. It is especially evident in this case. However, the number of errors is higher on the upper y-values.

The outputs and inputs are in accordance with each other. For larger solutal Grashof numbers, the input–output curve takes on a different shape, but still, the results are fine. The results follow the best-fit line. There is also a sufficiently large number of errors seen for lower y-values.

8 | CONCLUSION

This research investigates a hybrid nanofluid, comprising copper (Cu), and copper oxide (CuO) nanoparticles suspended in blood as the base fluid. The analysis considers the combined impacts of various factors such as viscous dissipation, gravity, an inclined external magnetic field, a highly porous medium, thermophoresis, Brownian motion, a heat source or sink, activation energy, and endothermic–exothermic chemical reactions. Graphical representations, along with appropriate justifications, are employed to discuss velocity, temperature, concentration, electroosmosis, heat transfer rate (Nusselt number), mass transfer rate (Sherwood number), skin friction coefficient, entropy generation, and Bejan number. The study yields several significant findings, including

(i) The fluid velocity increases by decreasing the magnetic field inclination, Reynolds number, and copper concentration and by increasing Helmholtz–Smoluchowski velocity.
(ii) The fluid temperature increased for the enhanced temperature ratio parameter, the temperature fitting constant, and by reducing the Forchheimer number, the activation energy parameter.
(iii) The concentration improves by raising the endothermic–exothermic reaction parameter, chemical reaction parameter, copper oxide concentration, and Schmidt number.
(iv) The electroosmosis profiles increased with the declining zeta potential of the right wall. It first declined and then inclined toward enhanced values of the electroosmosis parameter.
(v) Skin friction coefficient increases by increasing the Forchheimer, solutal Grashof, electroosmosis parameter, and Reynolds number.
(vi) The Nusselt number increases on the negative side by increasing the heat source and activation energy parameters and decreasing the endothermic–exothermic and Darcy numbers.
(vii) Sherwood number increases for reducing the temperature ratio, Schmidt fitting constant, and chemical reaction parameters.
(viii) Entropy generation improves the values of Brownian motion parameters and reduces the values of thermophoresis, activation energy, and endothermic–exothermic reaction parameters.
(ix) Bejan numbers increased by reducing the Brownian motion and endothermic–exothermic reaction parameters and increasing the thermophoresis and activation energy parameters.

A BRBP algorithm to predict the fluid's velocity, temperature, concentration, and electroosmosis properties is used and evaluated for its training state, performance, fit, regression, and error histogram plots for various flow parameters. Hybrid nanofluids find applications in various fields, such as electronic cooling, solar energy harvesting, and automobile engines. They have shown promising results in enhancing thermal conductivity and heat transfer performance. The computational time for neural network predictions signifies the speed at which the artificial intelligence model processes and predicts results. This efficiency is particularly relevant for real-time applications or scenarios where rapid analyses are crucial. On the other hand, the simulation time achieved with the BVP solver represents the computational cost of a more traditional numerical method. Understanding and comparing these times provide valuable insights into the relative strengths and limitations of both methodologies, aiding in the selection of the most appropriate approach for similar problems in the future.

NOMENCLATURE

(C_0, C_1) concentration at walls
(T_0, T_1) temperature at walls

(U^*, W^*)	velocity of HNF in (X^*, Y^*) direction
(X^*, Y^*)	fixed frame (in rectangular coordinates)
(u, w)	velocity of HNF in (x, y) direction
(x, y)	wave frame (in rectangular coordinates)
B_0	strength of uniform magnetic field
D_B	Brownian motion coefficient
D_T	thermophoretic diffusion coefficient
E_a	activation energy
E_x	electrokinetic body force
F_0	porous medium coefficient
T_{ave}	average temperature
c_p	specific heat
k^*	absorption coefficient
k_1	permeability of porous medium
k_b	Boltzmann constant
k_r	chemical reaction constant
n_0	bulk concentration
q_0	heat source/sink
β_c	volumetric concentration coefficient
β_t	volumetric thermal coefficient
γ	shear rate
ε_0	permittivity of free space
λ_1	ratio of relaxation to retardation times
λ_2	retardation time
ρ_e	electric charge density
ρ_p	density of nanoparticles
σ^*	Stefan–Boltzmann constant
$+H$	right cilia wall
hnf	hybrid nanofluid
C	concentration
F	time-average flow rate
$-H$	left cilia wall
S	stress tensor
T	temperature
c	wave speed
d	channel half width
e	electronic charge
f	fluid
g	gravitational acceleration
k	thermal conductivity
l	cilia length
n	fitting constant
nf	nanofluid
p	pressure
t	time
υ	kinematic viscosity
z	charge balance
α	eccentricity parameter
δ	wavenumber
ε	permittivity of medium
ζ	zeta potential
λ	wavelength

μ dynamic viscosity
ρ density
ς endothermic–exothermic reaction coefficient
σ electrical conductivity
τ effective heat capacity
ψ stream function
ω angle of magnetic field

ACKNOWLEDGMENTS

This project was supported by King Saud University, Deanship of Scientific Research, College of Science, Research Center.

CONFLICT OF INTEREST STATEMENT

The authors declare no conflicts of interest.

ORCID

Muhammad M. Bhatti https://orcid.org/0000-0002-3219-7579

REFERENCES

[1] Choi, S.U., Eastman, J.A.: Enhancing thermal conductivity of fluids with nanoparticles (No. ANL/MSD/CP-84938; CONF-951135-29). Argonne National Lab.(ANL), Argonne, IL (1995)
[2] Aytaç, İ., Tuncer, A.D., Khanlari, A., Variyenli, H.İ., Mantıcı, S., Güngör, L., Ünvar, S.: Investigating the effects of using MgO-CuO/water hybrid nanofluid in an evacuated solar water collector: a comprehensive survey. Therm. Sci. Eng. Prog. 39, 101688 (2023)
[3] Farooq, U., Waqas, H., Aldhabani, M.S., Fatima, N., Alhushaybari, A., Ali, M.R., Sadat R., Muhammad, T.: Modeling and computational framework of radiative hybrid nanofluid configured by a stretching surface subject to entropy generation: using Keller box scheme. Arab. J. Chem. 16(4), 104628 (2023)
[4] Abdollahi, S.A., Alizadeh, A.A., Zarinfar, M., Pasha, P.: Investigating heat transfer and fluid flow betwixt parallel surfaces under the influence of hybrid nanofluid suction and injection with numerical analytical technique. Alex. Eng. J. 70, 423–439 (2023)
[5] Kho, Y.B., Jusoh, R., Salleh, M.Z., Ariff, M.H., Zainuddin, N.: Magnetohydrodynamics flow of Ag-TiO2 hybrid nanofluid over a permeable wedge with thermal radiation and viscous dissipation. J. Magn. Magn. Mater. 565, 170284 (2023)
[6] Manzoor, U., Waqas, H., Farooq, U., Muhammad, T., Imran, M.: Entropy optimization of Marangoni flow of hybrid nanofluid under the influence of viscous dissipation and activation energy: with melting phenomenon. ZAMM-J. Appl. Math. Mech./Zeitschrift für Angewandte Mathematik und Mechanik 103, e202100416 (2023)
[7] Raju, S.: Dynamical dissipative and radiative flow of comparative an irreversibility analysis of micropolar and hybrid nanofluid over a Joule heating inclined channel. Sci. Rep. 13(1), 1–13 (2023)
[8] Ramesh, K., Warke, A.S., Kotecha, K., Vajravelu, K.: Numerical and artificial neural network modelling of magnetorheological radiative hybrid nanofluid flow with Joule heating effects. J. Magn. Magn. Mater. 570, 170552 (2023)
[9] Selimefendigil, F., Öztop, H.F.: Combined effects of using multiple porous cylinders and inclined magnetic field on the performance of hybrid nanoliquid forced convection. J. Magn. Magn. Mater. 565, 170137 (2023)
[10] Vijayalakshmi, P., Sivaraj, R.: Heat transfer analysis on micropolar alumina–silica–water nanofluid flow in an inclined square cavity with inclined magnetic field and radiation effect. J. Therm. Anal. Calorim. 148(2), 473–488 (2023)
[11] Surendar, R., Muthtamilselvan, M.: Nonlinear system synthesis via a quasiperiodic gravity sinusoidal modulation to suppress chaos in Ag–MgO/H2O hybrid nanofluid of actuator and sensor array. Arch Appl Mech, 93, 1–27 (2023)
[12] Rana, P., Gupta, V., Kumar, L.: Thermal instability analysis in magneto-hybrid nanofluid layer between rough surfaces with variable gravity and space-dependent heat source. Int. J. Mod. Phys. B, 38, 2450051 (2023)
[13] Khosravi, R., Zamaemifard, M., Safarzadeh, S., Passandideh-Fard, M., Teymourtash, A.R., Shahsavar, A.: Predicting entropy generation of a hybrid nanofluid in microchannel heat sink with porous fins integrated with high concentration photovoltaic module using artificial neural networks. Eng. Anal. Bound. Elem. 150, 259–271 (2023)
[14] Rashad, A.M., Nafe, M.A., Eisa, D.A.: Heat generation and thermal radiation impacts on flow of magnetic Eyring–Powell hybrid nanofluid in a porous medium. Arab. J. Sci. Eng. 48(1), 939–952 (2023)
[15] Sridhar, V., Khashi'ie, N.S., Ramesh, K.: Thermal and electroosmotic transport of blood-copper/platinum nanofluid in a microfluidic vessel with entropy analysis. Proc. Inst. Mech. Eng., Part E: J. Process Mech. Eng., 09544089231161306 (2023)
[16] Shahzadi, I., Duraihem, F.Z., Ijaz, S., Raju, C.S.K., Saleem, S.: Blood stream alternations by mean of electroosmotic forces of fractional ternary nanofluid through the oblique stenosed aneurysmal artery with slip conditions. Int. Commun. Heat Mass Transf. 143, 106679 (2023)

[17] Sajid, T., Jamshed, W., Eid, M.R., Altamirano, G.C., Aslam, F., Alanzi, A.M., Abd-Elmonem, A.: Magnetized Cross tetra hybrid nanofluid passed a stenosed artery with nonuniform heat source (sink) and thermal radiation: Novel tetra hybrid Tiwari and Das nanofluid model. J. Magn. Magn. Mater. 569, 170443 (2023)

[18] Mahmood, Z., Khan, U.: Unsteady three-dimensional nodal stagnation point flow of polymer-based ternary-hybrid nanofluid past a stretching surface with suction and heat source. Sci. Prog. 106(1), 00368504231152741 (2023)

[19] Abbas, M., Khan, N., Hashmi, M.S., Younis, J.: Numerically analysis of Marangoni convective flow of hybrid nanofluid over an infinite disk with thermophoresis particle deposition. Sci. Rep. 13(1), 5036 (2023)

[20] Madhukesh, J.K., Ramesh, G.K., Prasannakumara, B.C.: Convective thermal conditions and the thermophoretic effect's impacts on a hybrid nanofluid over a moving thin needle. Numer Methods Partial Differ Equ. 39(2), 1163–1184 (2023)

[21] Rashid, A., Dawar, A., Ayaz, M., Islam, S., Galal, A.M., Gul, H.: Homotopic solution of the chemically reactive magnetohydrodynamic flow of a hybrid nanofluid over a rotating disk with Brownian motion and thermophoresis effects. ZAMM-J. Appl. Math. Mech./Zeitschrift für Angewandte Mathematik und Mechanik 103, e202200262 (2023)

[22] Kalpana, G., Madhura, K.R., Kudenatti, R.B.: Magnetohydrodynamic boundary layer flow of hybrid nanofluid with the thermophoresis and Brownian motion in an irregular channel: a numerical approach. Eng. Sci. Technol., Int. J. 32, 101075 (2022)

[23] Ramzan, M., Shamshad, U., Rehman, S., Junaid, M.S., Saeed, A., Kumam, P.: Analytical simulation of Hall current and Cattaneo–Christov heat flux in Cross-hybrid nanofluid with autocatalytic chemical reaction: an engineering application of engine oil. Arab. J. Sci. Eng. 48(3), 3797–3817 (2023)

[24] Shah, S.A.A., Ahammad, N.A., Din, E.M.T.E., Gamaoun, F., Awan, A.U., Ali, B.: Bio-convection effects on prandtl hybrid nanofluid flow with chemical reaction and motile microorganism over a stretching sheet. Nanomaterials 12(13), 2174 (2022)

[25] Ullah, I., Alam, M.M., Rahman, M.M., Pasha, A.A., Jamshed, W., Galal, A.M.: Theoretical analysis of entropy production in exothermic/endothermic reactive magnetized nanofluid flow through curved porous space with variable permeability and porosity. Int. Commun. Heat Mass Transf. 139, 106390 (2022)

[26] Sharma, B.K., Gandhi, R., Mishra, N.K., Al-Mdallal, Q.M.: Entropy generation minimization of higher-order endothermic/exothermic chemical reaction with activation energy on MHD mixed convective flow over a stretching surface. Sci. Rep. 12(1), 17688 (2022)

[27] Jayaprakash, M.C., Alsulami, M.D., Shanker, B., Varun Kumar, R.S.: Investigation of Arrhenius activation energy and convective heat transfer efficiency in radiative hybrid nanofluid flow. Waves Random Complex Media, 1–13 (2022). https://doi.org/10.1080/17455030.2021.2022811

[28] Raza, Q., Qureshi, M.Z.A., Khan, B.A., Kadhim Hussein, A., Ali, B., Shah, N.A., Chung, J.D.: Insight into dynamic of mono and hybrid nanofluids subject to binary chemical reaction, activation energy, and magnetic field through the porous surfaces. Mathematics 10(16), 3013 (2022)

[29] Haq, I., Yassen, M.F., Ghoneim, M.E., Bilal, M., Ali, A., Weera, W.: Computational study of MHD Darcy–Forchheimer hybrid nanofluid flow under the influence of chemical reaction and activation energy over a stretching surface. Symmetry 14(9), 1759 (2022)

[30] Rani, S., Kathuria, I., Kumar, A., Kumar, D., Kumar, A., Kumar, S., Nandan, B. Srivastava, R.K.: Valorised polypropylene waste based reversible sensor for copper ion detection in blood and water. Environ. Res. 228, 115928 (2023)

[31] JP, C., Punnakkal, N., Vasu, S.P., Pradeep, A., Nair, B.G., Babu, T.S.: Zirconium copper oxide microflowers based non-enzymatic screen-printed electrochemical sensor for the detection of glucose in saliva, urine, and blood serum. Microchim. Acta 190(10), 390 (2023)

[32] Khan, U., Zaib, A., Khan, I., Nisar, K.S.: Insight into the dynamics of transient blood conveying gold nanoparticles when entropy generation and Lorentz force are significant. Int. Commun. Heat Mass Transf. 127, 105415 (2021)

[33] Rana, P., Ma, J., Zhang, Y., Chen, J., Gupta, G.: Finite element and neural computations for energy system containing conductive solid body and bottom circular heaters utilizing Ag–MgO (50: 50)/water hybrid nanofluid. J. Magn. Magn. Mater. 577, 170775 (2023)

[34] Rana, P., Kumar, A., Gupta, G.: Impact of different arrangements of heated elliptical body, fins and differential heater in MHD convective transport phenomena of inclined cavity utilizing hybrid nanoliquid: artificial neutral network prediction. Int. CoCmun. Heat Mass Transf. 132, 105900 (2022)

[35] Kanti, P.K., Sharma, P., Koneru, B., Banerjee, P., Jayan, K.D.: Thermophysical profile of graphene oxide and MXene hybrid nanofluids for sustainable energy applications: Model prediction with a Bayesian optimized neural network with K-cross fold validation. FlatChem, 39, 100501 (2023)

[36] Çolak, A.B.: Prediction of viscous dissipation effects on magnetohydrodynamic heat transfer flow of copper-poly vinyl alcohol Jeffrey nanofluid through a stretchable surface using artificial neural network with Bayesian Regularization. Chem. Thermodyn. Thermal Anal. 6, 100056 (2022)

[37] Awan, S.E., Awais, M., Raja, M.A.Z., Rehman, S.U., Shu, C.M.: Bayesian regularization knack-based intelligent networks for thermo-physical analysis of 3D MHD nanofluidic flow model over an exponential stretching surface. Eur. Phys. J. Plus 138(1), 2 (2023)

[38] Mahmood, T., Ali, N., Chaudhary, N.I., Cheema, K.M., Milyani, A.H., Raja, M.A.Z.: Novel adaptive Bayesian regularization networks for peristaltic motion of a third-grade fluid in a planar channel. Mathematics 10(3), 358 (2022)

[39] Shoaib, M., Nisar, K.S., Zahoor Raja, M.A., Tariq, Y., Tabassum, R., Rafiq, A.: Intelligent computing system-based Bayesian regularization backpropagation for viscous dissipative transport of a ferrofluid (Fe_3O_4) mode. Waves Random Complex Media, 1–19 (2022). https://doi.org/10.1080/17455030.2022.2154868

[40] Sundar, L.S., Mewada, H.K.: Experimental entropy generation, exergy efficiency and thermal performance factor of CoFe2O4/water nanofluids in a tube predicted with ANFIS and MLP models. Int. J. Therm. Sci. 190, 108328 (2023)

[41] Kamsuwan, C., Wang, X., Piumsomboon, P., Pratumwal, Y., Otarawanna, S., Chalermsinsuwan, B.: Artificial neural network prediction models for nanofluid properties and their applications with heat exchanger design and rating simulation. Int. J. Therm. Sci. 184, 107995 (2023)

[42] Hassan, M., Rizwan, M., Bhatti, M.M.: Investigating the influence of temperature-dependent rheological properties on nanofluid behavior in heat transfer. Nanotechnology 34(50), 505404 (2023)

[43] Esfe, M.H., Toghraie, D., Amoozadkhalili, F.: Optimization and design of ANN with Levenberg-Marquardt algorithm to increase the accuracy in predicting the viscosity of SAE40 oil-based hybrid nano-lubricant. Powder Technol. 415, 118097 (2023)

[44] Kolsi, L., Selimefendigil, F., Gasmi, H., Alshammari, B.M.: Conjugate heat transfer analysis for cooling of a conductive panel by combined utilization of nanoimpinging jets and double rotating cylinders. Nanomaterials 13(3), 500 (2023)

[45] Hoang, A.T., Nižetić, S., Ong, H.C., Tarelko, W., Le, T.H., Chau, M.Q., Nguyen, X.P.: A review on application of artificial neural network (ANN) for performance and emission characteristics of diesel engine fueled with biodiesel-based fuels. Sustain. Energy Technol. Assess. 47, 101416 (2021)

[46] Sleigh, M.A.: The biology of Cilia and Flagella: international series of monographs on pure and applied biology: zoology, vol. 12, vol. 12. Elsevier, Kent (2016)

[47] Esfe, M.H., Motallebi, S.M., Hatami, H., Amiri, M.K., Esfandeh, S., Toghraie, D.: Optimization of density and coefficient of thermal expansion of MWCNT in thermal oil nanofluid and modeling using MLP and response surface methodology. Tribol. Int. 183, 108410 (2023)

[48] Song, Y.Q., Obideyi, B.D., Shah, N.A., Animasaun, I.L., Mahrous, Y.M., Chung, J.D.: Significance of haphazard motion and thermal migration of alumina and copper nanoparticles across the dynamics of water and ethylene glycol on a convectively heated surface. Case Stud. Therm. Eng. 26, 101050 (2021)

[49] Cao, W., Animasaun, I.L., Yook, S.J., Oladipupo, V.A., Ji, X.: Simulation of the dynamics of colloidal mixture of water with various nanoparticles at different levels of partial slip: ternary-hybrid nanofluid. Int. Commun. Heat Mass Transf. 135, 106069 (2022)

[50] Saleem, N., Munawar, S.: Significance of synthetic cilia and Arrhenius energy on double diffusive stream of radiated hybrid nanofluid in microfluidic pump under ohmic heating: an entropic analysis. Coatings 11(11), 1292 (2021)

[51] Adnan, Abbas, W., Bani-Fwaz, M.Z., Asogwa, K.K.: Thermal efficiency of radiated tetra-hybrid nanofluid [(Al2O3-CuO-TiO2-Ag)/water] tetra under permeability effects over vertically aligned cylinder subject to magnetic field and combined convection. Sci. Prog., 106(1), 00368504221149797 (2023)

[52] Munawar, S., Saleem, N., Tripathi, D.: Cilia and electroosmosis induced double diffusive transport of hybrid nanofluids through microchannel and entropy analysis. Int. J. Nonlinear Modell. Sci. Eng. 12(1), 20220287 (2023)

[53] Ramesh, K., Prakash, J.: Thermal analysis for heat transfer enhancement in electroosmosis-modulated peristaltic transport of Sutter by nanofluids in a microfluidic vessel. J. Therm. Anal. Calorim. 138, 1311–1326 (2019)

[54] Sharma, B.K., Khanduri, U., Mishra, N.K., Mekheimer, K.S.: Combined effect of thermophoresis and Brownian motion on MHD mixed convective flow over an inclined stretching surface with radiation and chemical reaction. Int. J. Mod. Phys. B 37, 2350095 (2022)

[55] Saleem, N., Munawar, S., Tripathi, D.: Entropy analysis in ciliary transport of radiated hybrid nanofluid in presence of electromagnetohydrodynamic and activation energy. Case Stud. Therm. Eng. 28, 101665 (2021)

[56] Sharma, B.K., Kumawat, C., Makinde, O.D.: Hemodynamical analysis of MHD two phase blood flow through a curved permeable artery having variable viscosity with heat and mass transfer. Biomech. Model. Mechanobiol. 21(3), 797–825 (2022)

[57] Sharma, B.K., Poonam, Chamkha, A.J.: Effects of heat transfer, body acceleration and hybrid nanoparticles (Au–Al2O3) on MHD blood flow through a curved artery with stenosis and aneurysm using hematocrit-dependent viscosity. Waves Random Complex Media, 1–31 (2022). https://doi.org/10.1080/17455030.2022.2125597

[58] Sharma, B.K., Kumar, A., Gandhi, R., Bhatti, M.M., Mishra, N.K.: Entropy generation and thermal radiation analysis of EMHD Jeffrey nanofluid flow: applications in solar energy. Nanomaterials 13(3), 544 (2023)

[59] Gandhi, R., Sharma, B.K., Mishra, N.K., Al-Mdallal, Q.M.: Computer simulations of EMHD Casson nanofluid flow of blood through an irregular stenotic permeable artery: application of Koo-Kleinstreuer-Li correlations. Nanomaterials 13(4), 652 (2023)

[60] Gandhi, R., Sharma, B.K., Kumawat, C., Bég, O.A.: Modeling and analysis of magnetic hybrid nanoparticle (Au-Al2O3/blood) based drug delivery through a bell-shaped occluded artery with joule heating, viscous dissipation and variable viscosity effects. Proc. Inst. Mech. Eng., Part E: J. Process Mech. Eng. 236(5), 2024–2043 (2022)

[61] Sharma, B.K., Khanduri, U., Mishra, N.K., Chamkha, A.J.: Analysis of Arrhenius activation energy on magnetohydrodynamic gyrotactic microorganism flow through porous medium over an inclined stretching sheet with thermophoresis and Brownian motion. Proc. Inst. Mech. Eng., Part E: J. Process Mech. Eng. 237, 09544089221128768 (2022)

[62] Sharma, B.K., Gandhi, R.: Combined effects of Joule heating and non-uniform heat source/sink on unsteady MHD mixed convective flow over a vertical stretching surface embedded in a Darcy-Forchheimer porous medium. Propuls. Power Res. 11(2), 276–292 (2022)

[63] Khanduri, U., Sharma, B.K.: Mathematical analysis of Hall effect and hematocrit dependent viscosity on Au/GO-blood hybrid nanofluid flow through a stenosed catheterized artery with thrombosis. In: Advances in Mathematical Modelling, Applied Analysis and Computation: Proceedings of ICMMAAC 2022, pp. 121–137. Springer Nature Switzerland, Cham (2023)

[64] Gandhi, R., Sharma, B.K.: Modelling pulsatile blood flow using Casson fluid model through an overlapping stenotic artery with Au-Cu hybrid nanoparticles: varying viscosity approach. In: Advances in Mathematical Modelling, Applied Analysis and Computation: Proceedings of ICMMAAC 2022, pp. 155–176. Springer Nature Switzerland, Cham (2023)

[65] Zhang, L., Bhatti, M.M., Michaelides, E.E., Ellahi, R.: Characterizing quadratic convection and electromagnetically induced flow of couple stress fluids in microchannels. Qual. Theory Dyn. Syst. 23(1), 35 (2024)

[66] Bhatti, M.M., Bég, O.A., Kuharat, S.: Electromagnetohydrodynamic (EMHD) convective transport of a reactive dissipative carreau fluid with thermal ignition in a non-Darcian vertical duct. Numer. Heat Transf. A Appl. 1–31 (2023). https://doi.org/10.1080/10407782.2023.2284333

How to cite this article: Sharma, P., Sharma, B.K., Mishra, N.K., Almohsen, B., Bhatti, M.M.: Electroosmotic Microchannel Flow of Blood conveying Copper and cupric nanoparticles: Ciliary motion experiencing entropy generation using Backpropagated Networks. Z Angew Math Mech. 104, e202300442 (2024). https://doi.org/10.1002/zamm.202300442